Oceanic forcing of penultimate deglacial and last interglacial sea-level rise

Ocean forcing of penultimate deglacial and last interglacial sea-level rise

Peter U. Clark[1,9,*,#], Feng He[2,*], Nicholas R. Golledge[3,4], Jerry X. Mitrovica[5], Andrea Dutton[6], Jeremy S. Hoffman[7], Sarah Dendy[8]

[1]College of Earth, Ocean, and Atmospheric Sciences, Oregon State University, Corvallis, OR 97331, USA. [2]Center for Climatic Research, Nelson Institute for Environmental Studies, University of Wisconsin–Madison, Madison, WI 53706, USA. [3]Antarctic Research Centre, Victoria University of Wellington, Wellington 6140, New Zealand. [4] GNS Science, Avalon, Lower Hutt 5011, New Zealand. [5]Department of Earth and Planetary Sciences, Harvard University, Cambridge, MA, 02138. [6]Department of Geological Sciences, University of Florida, Gainesville, FL 32611, USA. [7]Science Museum of Virginia, 2500 West Broad Street, Richmond, VA 23220-2057, USA. [8]Department of Geology, University of Illinois, Urbana-Champaign, IL 61801, USA. [9]School of Geography and Environmental Sciences, University of Ulster, Coleraine, Northern Ireland BT52 1SA, UK. *These authors contributed equally to this work. #email: clarkp@onid.orst.edu

Sea-level histories during the two most recent deglacial-interglacial intervals experienced significant differences[1-3] despite both periods having similar changes in global mean temperature[4,5] and forcing from greenhouse gases[6]. Although the last interglaciation (LIG) experienced stronger boreal summer insolation forcing than during the present interglaciation[7], understanding why LIG global mean sea level may have been 6-9 m higher than present has proven particularly challenging[2]. During glacial as well as interglacial periods, extensive areas of polar ice sheets were grounded below sea level, with grounding lines and fringing ice shelves extending onto continental shelves[8], suggesting that oceanic forcing by subsurface warming may also have contributed to ice-sheet loss[9-12] analogous to ongoing changes by the Antarctic[13,14] and Greenland[15] ice sheets. Such forcing would have been especially effective during glacial periods when the Atlantic Meridional Overturning Circulation (AMOC) experienced large variations on millennial timescales[16], with a reduction of the AMOC causing subsurface warming throughout much of the Atlantic basin[9,12,17]. Here we show that greater subsurface warming induced by the longer duration of reduced AMOC during the penultimate deglaciation can explain the more-rapid sea-level rise than during the last deglaciation. This greater forcing also contributed to excess loss from the Greenland and Antarctic ice sheets during the LIG, causing global mean sea level to rise at least 4 m above modern. When accounting for the combined influences of penultimate and last-interglacial deglaciation on glacial isostatic adjustment, this excess loss of polar ice during the LIG can explain much of the relative sea level recorded by fossil coral reefs and speleothems at intermediate- and far-field sites.

Climate evolution over the last two terminations shares a number of similarities (Extended Data Fig. 1). Proxy records of ocean circulation show that the last two terminations were accompanied by large reductions of the AMOC. Climate responses to these reductions show the characteristic bi-polar seesaw due to reduced northerly ocean heat transport and the weakening of the Asian monsoon due to the cooling of the Northern Hemisphere. Other similarities include an increase in the rate of sea-level rise when the AMOC begins to decrease and the occurrence of a Heinrich event during the period of reduced AMOC. Similar climate changes accompanied earlier terminations over the last 640 ka[18], suggesting that an AMOC reduction is a characteristic feature of these periods of rapid deglaciation.

There are also several notable differences between the last two terminations (Extended Data Figs. 1, 2). First, proxy data suggest that the AMOC during T-II remained in a reduced state for ~7,000 years before recovering at the start of the LIG. In contrast, during T-I, the AMOC only remained weak for ~3,500 years before recovering to nearly full strength during the 1,500-year Bølling-Allerød warm interval. It then decreased again during the 1,200-year Younger Dryas cold interval, with its final recovery at the start of the present interglaciation. Second, the full T-II sea-level rise occurred during the 7-kyr sustained "one-step" period of reduced AMOC, whereas only ~50% of the T-I sea-level rise occurred during the ~6.5-kyr "two-step" period of reduced AMOC[3] (Fig. 1). Third, ice-rafted debris (IRD) suggests that Heinrich event 11 (H11), which is nearly twice as long as Heinrich event 1 (H1), was sourced from more than just the Hudson Strait Ice Stream (HSIS), which was the primary source for H1[19].

A transient simulation of T-I climate used an atmosphere-ocean general circulation model (the National Center for Atmospheric Research Community Climate System Model version 3; NCAR CCSM3) forced by changes in insolation, CO_2, ice sheets, and freshwater fluxes that, while

not in full agreement with reconstructions, were designed to cause the two-step reduction of the AMOC[17] (Fig. 1k). The simulation successfully captured many aspects of the climate evolution through T-I as recorded by proxy records[17,20,21]. Among the responses to the AMOC reduction was subsurface warming throughout much of the Atlantic basin[17] (Fig. 1k, 1l), which is supported by proxy temperature records from intermediate-depth (1,000-1,500 m) North Atlantic core sites[12].

We used the same climate model to conduct a transient simulation that spans T-II and the LIG (140-115 ka) (Methods). We applied freshwater forcing consistent with reconstructions that reproduced the 7-kyr "one-step" reduction in the AMOC suggested by proxy records of ocean circulation (Extended Data Figs. 1,3) in order to quantify associated changes in subsurface temperatures during T-II and into the LIG and thus allow direct comparison with subsurface warming simulated for T-I.

Fig. 1 compares forcing of ice-sheet surface mass balance from insolation, greenhouse gases (GHGs), and low-latitude Pacific sea-surface temperatures (SSTs) for T-II and T-I to representative examples of the simulated oceanic forcing at sites in the North (30°W, 45°N) (Fig. 1e, 1k) and South Atlantic (45°W, 70°S) (Fig. 1f, 1l). Changes in GHGs and SSTs are similar during the two terminations, with increases of ~2 W m^{-2} from GHGs and ~2°C warming from low-latitude Pacific SSTs, which strongly influence Northern Hemisphere ice-sheet surface mass balance[10]. Despite these similarities, sea level reached modern by the end of T-II while it remained ~50% below modern at the end of T-I (Fig. 1a, 1g). Some have attributed the faster rate of sea-level rise during T-II to the greater boreal summer insolation forcing[3], but that forcing only exceeds that of T-I after the majority (~80 m) of T-II sea-level rise had occurred (Fig. 1a, 1b, Extended Data Fig. 2). Otherwise, insolation forcing during the first 8,000 years of each termination is

84 similar (~55 W m^2), whereas the associated 80 m of sea-level rise during T-II is much greater than
85 the ~35 m during T-I.

86 We attribute this contrast in sea-level response to the similar radiative forcing and
87 temperature changes of the last two terminations to the greater subsurface warming during T-II
88 associated with the "one-step" reduction in the AMOC than during the T-I "two-step" reduction,
89 leading to greater oceanic forcing of marine ice-sheet margins in the North (Fig. 1e, 1k, Extended
90 Data Fig. 4) and South (Fig. 1f, 1l, Extended Data Fig. 4) Atlantic. Moreover, the Eurasian Ice
91 Sheet during the Penultimate Glacial Maximum (PGM, ~140 ka) was larger than during the Last
92 Glacial Maximum (LGM, ~21 ka), with most of the excess mass located in low-lying areas south-
93 southeast of the glaciated Barents and Kara Seas[22] that, from isostatic depression, was also marine
94 based (Extended Data Fig. 5). We thus hypothesize that collapse of this large marine-based ice
95 complex triggered by oceanic forcing would have also contributed to the rapid T-II sea-level rise,
96 with the associated IRD contribution to H11 diluting the contribution from the HSIS[19]. In general,
97 this greater FW flux from deglaciating Northern Hemisphere ice sheets during T-II provided an
98 important positive feedback on that deglaciation through its influence on the AMOC and
99 subsurface temperatures.

100 Fig. 2 compares forcings during the last two interglaciations. Peak global mean SSTs were
101 similar (Fig. 2d, 2i) while LIG radiative forcing from CO_2 was only slightly higher (~0.25 W m^{-2})
102 than during the present interglaciation (Fig. 2c, 2j). The main difference is in the higher boreal and
103 lower austral summer insolation forcing during the LIG (Fig. 2b, 2h). Modeling studies show that
104 this forcing would cause excess mass loss from the Greenland Ice Sheet during the LIG, but the
105 estimated 1-3 m of global mean sea-level equivalent (GMSLE) is too small to explain the LIG
106 highstand, thus requiring a contribution from the Antarctic Ice Sheet[2]. Lower austral summer

insolation forcing during the LIG (Fig. 2b), however, results in surface cooling over most of Antarctica, suggesting an important role for oceanic forcing, with warming hypothesized to originate from an AMOC reduction during the LIG[11] or from a lagged ice-sheet response to warming from a change in the strength and/or position of the Southern Ocean westerlies associated with the T-II AMOC reduction[3]. One ice-sheet model simulates up to 6.7 m of sea-level rise when specifying a uniform increase of Southern Ocean temperatures by 3˚C[11].

Our transient climate simulation shows that T-II oceanic forcing in the Southern Ocean as well as the North Atlantic continued into the early LIG (Fig. 2e, 2f, Extended Data Fig. 4). We use the Parallel Ice Sheet Model (PISM) to assess the response of the Antarctic and Greenland ice sheets to this oceanic as well as surface forcing through T-II and into the LIG as simulated by our transient climate run (Methods). The Greenland Ice Sheet starts to deglaciate from its PGM extent when adjacent ocean temperatures begin to warm at ~137.5 ka (Fig. 1e, Fig. 3g). It reaches its present extent at 131.5 ka and then loses an additional 0.88 m GMSLE by 119.5 ka largely by oceanic forcing of those sectors of the ice sheet that remain marine based, causing drawdown of the ice-sheet interior (Fig. 3c). The majority (3.42 m) of the total sea-level rise (3.88 m) occurs between 136-129 ka (Fig. 3g), corresponding to the period of rapid rise in global mean sea level (GMSL) (Fig. 1a). Sensitivity tests in which ocean temperatures are held constant at either PGM or LIG values show that the simulated deglaciation is controlled entirely by oceanic forcing (Methods, Extended Data Fig. 6), supporting our hypothesis that oceanic forcing contributed to deglaciation of other Northern Hemisphere ice sheets (Extended Data Fig. 4).

Our simulations also show that the major deglacial phase of the Antarctic Ice Sheet from its PGM extent closely coincides with the onset of warming of adjacent ocean temperatures at ~137.5 ka induced by the AMOC slowdown (Fig. 1f, Fig. 3g). In particular, the ice sheet retreats

130 to its present extent at ~128 ka, with the majority (6.25 m) of the total (6.65 m) sea-level rise also
131 occurring during the rapid T-II rise in global sea level (Fig. 3g). Sea-level rise then slows beginning
132 at 128 ka, followed by an acceleration starting at 126.5 ka, with a total of 2.99 m of LIG sea-level
133 rise occurring by 116 ka (Fig. 3g). The majority of this LIG deglaciation is associated with collapse
134 of the Amundsen Sea sector of the West Antarctic Ice Sheet (WAIS) (Fig. 3e) largely in response
135 to oceanic forcing (Extended Data Fig. 6), similar to what is suggested by observed recent changes
136 and projected for future ice-sheet recession in this area[13,14]. This destabilization leads to retreat
137 that continues after the period of peak oceanic forcing at a rate that is determined largely by the
138 retrograde gradient of the bed beneath WAIS, followed by a slowing of retreat as the Southern
139 Ocean cools (Fig. 2f).

140 We next apply an ice-age sea-level model[23] to predict how our simulated changes in LIG
141 ice-sheet mass would be recorded at three widely distributed sites with well-dated corals that
142 provide minimum estimates of relative sea level (RSL) during the LIG[24,25], and a speleothem
143 record that bounds RSL during the same period[26] (Methods). Of the five adopted ice histories, the
144 two (LAM and HYB) based on studies that use a significantly larger Eurasian Ice Sheet during the
145 PGM relative to the LGM[22,27] best predict RSL histories during the LIG that are consistent with
146 the elevation of the corals from the Bahamas, Western Australia and the Seychelles (Fig. 4a-c,
147 Extended Data Fig. 7). However, all simulations tend to underestimate the first half (prior to 122
148 ka) of the LIG RSL inferred from the speleothem record in Mallorca (Fig. 4d, Extended Data Fig.
149 7).

150 In the absence of melting of polar ice during the LIG, predictions of RSL at the Bahamas
151 and at Mallorca would show a monotonic rise, while those at the Seychelles and Western Australia
152 would tend to show a monotonic fall[28]. Our ice-sheet simulations, however, are characterized by

153 excess melt from WAIS (relative to present day) that increases from 0 to 3 m GMSLE between
154 127 ka and 124 ka (Fig. 3g). This signal is responsible for the accentuated RSL rise over the same
155 period in the prediction for Bahamas and Mallorca and the reversal in the RSL trend at Western
156 Australia and the Seychelles (Fig. 4).

157 Our results do not account for several other processes that may have caused LIG global
158 mean and relative sea level to have been even higher than modeled here. For example, our
159 atmospheric modeling may underestimate surface melting around the lower-elevation margins of
160 the Greenland Ice Sheet. The greater boreal summer insolation forcing during the LIG relative to
161 the present interglaciation likely caused an even greater loss of glaciers, which today account for
162 0.41 m GMSLE. Warmer-than-present LIG temperatures would have caused additional
163 thermosteric sea-level rise[5]. Finally, we note that any additional melt near the start of the LIG
164 would change the preferred Earth models identified in our analysis (Methods). LIG RSL can also
165 be influenced by dynamic topography due to mantle convection, introducing meter-scale
166 displacement on these 10^5-year timescales[29].

167 In summary, several lines of evidence suggest that the greater oceanic forcing during T-II
168 than during T-I, as simulated by our climate modeling, contributed to the more-rapid sea-level rise
169 during T-II. First, forcing of ice-sheet surface mass balance was similar during the two
170 terminations, indicating that an additional forcing was required to explain the differences in rates
171 of sea-level rise. Second, our GIA modeling demonstrates that the larger PGM Eurasian ice sheet
172 caused a significantly larger fraction of the ice-sheet bed to be below sea level, and thus be more
173 vulnerable to oceanic forcing, than during T-I. Third, our ice-sheet modeling shows that >85% of
174 the volume loss of the PGM Greenland and Antarctic ice sheets to their present sizes occurs in
175 response to oceanic forcing during T-II. Although additional modeling of the deglaciation of the

former NH ice sheets during T-II will be required to further support this hypothesis, our ice-sheet modeling does show that oceanic forcing was the primary driver of excess ice loss from the Greenland and Antarctic ice sheets during the LIG. Our sea-level predictions demonstrate that the modeled 4 m of GMSLE from LIG deglaciation of Greenland and Antarctic ice sheets may explain much of the LIG RSL at intermediate- and far-field sites when GIA from T-II deglaciation is included, although additional melt is required to fully reconcile these data.

1 Waelbroeck, C. *et al.* Sea-level and deep water temperature changes derived from benthic foraminifera isotopic records. *Quaternary Science Reviews* **21**, 295-305 (2002).

2 Dutton, A. *et al.* Sea-level rise due to polar ice-sheet mass loss during past warm periods. *Science* **349**, doi:10.1126/science.aaa4019 (2015).

3 Marino, G. *et al.* Bipolar seesaw control on last interglacial sea level. *Nature* **522**, 197-201, doi:10.1038/nature14499 (2015).

4 Marcott, S. A., Shakun, J. D., Clark, P. U. & Mix, A. C. A reconstruction of regional and global temperature for the past 11,300 years. *Science* **339**, 1198-1201 (2013).

5 Hoffman, J. S., Clark, P. U., Parnell, A. C. & He, F. Regional and global sea-surface temperatures during the last interglaciation. *Science* **355**, 276-279, doi:10.1126/science.aai8464 (2017).

6 Kohler, P., Nehrbass-Ahles, C., Schmitt, J., Stocker, T. F. & Fischer, H. A 156 kyr smoothed history of the atmospheric greenhouse gases CO2, CH4, and N2O and their radiative forcing. *Earth System Science Data* **9**, doi:10.5194/essd-9-363-2017 (2017).

7 Berger, A. & Loutre, M.-F. Insolation values for the climate of the last 10 million years. *Quaternary Science Reviews* **10**, 297-317 (1991).

8 Hughes, T., Denton, G. H. & Grosswald, M. G. Was There a Late-Wurm Arctic Ice Sheet. *Nature* **266**, 596-602, doi:DOI 10.1038/266596a0 (1977).

9 Shaffer, G., Olsen, S. M. & Bjerrum, C. J. Ocean subsurface warming as a mechanism for coupling Dansgaard-Oeschger climate cycles and ice-rafting events. *Geophysical Research Letters* **31**, L24202, doi:24210.21029/22004GL020968 (2004).

10 Clark, P. U., Hostetler, S. W., Pisias, N. G., Schmittner, A. & Meisner, K. J. in *Ocean Circulation: Mechanisms and Impacts* Vol. 173 (eds A. Schmittner, J. Chiang, & S. Hemming) 209-246 (American Geophysical Union, Geophysical Monograph, 2007).

11 DeConto, R. M. & Pollard, D. Contribution of Antarctica to past and future sea-level rise. *Nature* **531**, 591-597, doi:10.1038/nature17145 (2016).

12 Marcott, S. A. *et al.* Ice-shelf collapse from subsurface warming as a trigger for Heinrich events. *Proceedings of the National Academy of Sciences of the United States of America* **108**, 13415-13419 (2011).

13 Joughin, I., Smith, B. E. & Medley, B. Marine ice sheet collapse potentially under way for the Thwaites Glacier basin, West Antarctica. *Science* **344**, 735-738 (2014).

14 Rignot, E., Mouginot, J., Morlighem, M., Seroussi, H. & Scheuchl, B. Widespread, rapid grounding line retreat of Pine Island, Thwaites, Smith, and Kohler glaciers, West Antarctica, from 1992 to 2011. *Geophysical Research Letters* **41**, 3502-3509 (2014).
15 Wood, M. *et al.* Ocean-induced melt triggers glacier retreat in northwest Greenland. *Geophysical Research Letters* **45**, 8334-8342, doi:10.1029/2018gl078024 (2018).
16 Bohm, E. *et al.* Strong and deep Atlantic meridional overturning circulation during the last glacial cycle. *Nature* **517**, 73-76, doi:10.1038/nature14059 (2015).
17 Liu, Z. *et al.* Transient simulation of last deglaciation with a new mechanism for Bolling-Allerod warming. *Science* **325**, 310-314 (2009).
18 Cheng, H. *et al.* The Asian monsoon over the past 640,000 years and ice age terminations. *Nature* **534**, 640-646, doi:10.1038/nature18591 (2016).
19 Obrochta, S. P. *et al.* Climate variability and ice-sheet dynamics during the last three glaciations. *Earth and Planetary Science Letters* **406**, 198-212, doi:10.1016/j.epsl.2014.09.004 (2014).
20 Shakun, J. D. *et al.* Global warming preceded by increasing carbon dioxide concentrations during the last deglaciation. *Nature* **484**, 49-55 (2012).
21 He, F. *et al.* Northern Hemisphere forcing of Southern Hemisphere climate during the last deglaciation. *Nature* **494**, 81-85 (2013).
22 Lambeck, K. *et al.* Constraints on the Late Saalian to early Middle Weichselian ice sheet of Eurasia from field data and rebound modelling. *Boreas* **35**, 539-575, doi:Doi 10.1080/03009480600781875 (2006).
23 Kendall, R. A., Mitrovica, J. X. & Milne, G. A. On post-glacial sea level - II. Numerical formulation and comparative results on spherically symmetric models. *Geophysical Journal International* **161**, 679-706 (2005).
24 Dutton, A. & Lambeck, K. Ice volume and sea level during the Last Interglacial. *Science* **337**, 216-219, doi:10.1126/science.1205749 (2012).
25 Dutton, A., Webster, J. M., Zwartz, D., Lambeck, K. & Wohlfarth, B. Tropical tales of polar ice: evidence of Last Interglacial polar ice sheet retreat recorded by fossil reefs of the granitic Seychelles islands. *Quaternary Science Reviews* **107**, 182-196, doi:10.1016/j.quascirev.2014.10.025 (2015).
26 Polyak, V. J. *et al.* A highly resolved record of relative sea level in the western Mediterranean Sea during the last interglacial period. *Nature Geoscience* **11**, 860-864, doi:10.1038/s41561-018-0222-5 (2018).
27 Colleoni, F., Wekerle, C., Naslund, J. O., Brandefelt, J. & Masina, S. Constraint on the penultimate glacial maximum Northern Hemisphere ice topography (approximate to 140 kyrs BP). *Quaternary Science Reviews* **137**, 97-112, doi:10.1016/j.quascirev.2016.01.024 (2016).
28 Dendy, S., Austermann, J., Creveling, J. R. & Mitrovica, J. X. Sensitivity of Last Interglacial sea-level high stands to ice sheet configuration during Marine Isotope Stage 6. *Quaternary Science Reviews* **171**, 234-244, doi:10.1016/j.quascirev.2017.06.013 (2017).
29 Austermann, J., Mitrovica, J. X., Huybers, P. & Rovere, A. Detection of a dynamic topography signal in last interglacial sea-level records. *Science Advances* **3**, doi:10.1126/sciadv.1700457 (2017).

Acknowledgments This work was funded by the US National Science Foundation (NSF) through grants AGS-1503032 (to P.U.C.), AGS-1502990 (to F.H.) OCE-1702684 (to J.X.M.), and 1559040 (to A.D.); the NOAA Climate and Global Change Postdoctoral Fellowship program, administered by the University Corporation for Atmospheric Research (to F.H.); contract VUW1501 from the Royal Society Te Aparangi with support from the Antarctic Research Centre, Victoria University of Wellington (to N.R.G.); contract CO5X1001 to GNS Science from the Ministry for Business, Innovation and Employment (to N.R.G.); and Harvard University (J.X.M.). We acknowledge high-performance computing support from Yellowstone (ark:/85065/d7wd3xhc) provided by NCAR's Computational and Information Systems Laboratory, sponsored by the NSF. This research used resources of the Oak Ridge Leadership Computing Facility at the Oak Ridge National Laboratory, which is supported by the Office of Science of the US Department of Energy under Contract No. DE-AC05-00OR22725. PISM is supported by NASA grants NNX13AM16G and NNX13AK27G. We thank Jason Box, Christo Buizert, and Anais Orsi for discussions.

Author contributions F.H. performed the GCM modeling; N.R.G. performed the ice-sheet modeling; J.X.M. performed the sea-level modeling with help from S.D.; P.U.C., A.D. and J.S.H. performed the data analysis; P.U.C., F.H., N.R.G., and J.X.M. wrote the manuscript; all authors discussed the results and contributed towards improving the final manuscript.

Competing interests The authors declare no competing interests.

Correspondence and requests for materials should be addressed to P.U.C.

Fig. 1. Sea-level change and climate forcings during the penultimate and last deglaciations. **a, g,** Records of relative and global mean sea level (Methods, Extended Data Fig. 2). Uncertainty on blue line is 1σ; uncertainty on coral data (circles) is 2σ. **b, h,** June 21 insolation for 65°N[7]. **c, i,** Radiative forcing from greenhouse gases (CO_2, CH_4, and N_2O)[6]. Uncertainty is square root of the sum of squares of the uncertainties of the individual greenhouse gases. **d, j,** Tropical (23.5°N-S) mean annual sea-surface temperature stack with 2 s.d. relative to the HadISST1.1 1870–1889 data[4,5]. **e, k,** Changes in the model maximum Atlantic meridional overturning transport (below 500 m) (black line) and of temperature as a function of time and depth at 30°W, 45°N relative to 140 ka (**e**) and 22 ka[17] (**k**) as simulated by the NCAR CCSM3 (Methods). **f, l,** Evolution of temperature as a function of time and depth at 45°W, 70°S relative to 140 ka (**f**) and 22 ka[17] (**l**) as simulated by the NCAR CCSM3 (Methods).

Fig. 2. Sea level and climate forcings during the last and present interglaciations. a, g, Records of relative and global mean sea level (Methods, Extended Data Fig. 2). Uncertainty on coral data (circles) is 2σ. **b, h,** June 21 insolation for 65°N[7]. **c, i,** Radiative forcing from greenhouse gases (CO_2, CH_4, and N_2O)[6]. Uncertainty is the square root of the sum of squares of the uncertainties of the individual greenhouse gases. **d, j,** Global mean annual sea-surface temperature stack with 2 s.d. relative to the HadISST1.1 1870–1889 data[4,5]. **e, k,** Evolution of temperature as a function of time and depth at 30°W, 45°N relative to 140 ka (**e**) and 22 ka[17] (**k**) as simulated by the NCAR CCSM3 (Methods). **f, l,** Evolution of temperature relative to 140 ka as a function of time and depth at 45°W, 70°S relative to 140 ka (**f**) and 22 ka[17] (**l**) as simulated by the NCAR CCSM3 (Methods).

Fig. 3. Simulations of the Greenland and Antarctic ice sheets. a, The Greenland Ice Sheet at the Penultimate Glacial Maximum. Logarithmic scale bar for velocity fields shown by color scheme; contours on ice sheet are for surface elevation in meters. **b,** The Greenland Ice Sheet at 116 ka. Logarithmic scale bar for velocity fields shown by color scheme; contours on ice sheet are for surface elevation in meters. **c,** Difference in thickness of the Greenland Ice Sheet between 116 ka and present day. Contours on ice surface and color scheme show change in thickness. **d,** The Antarctic Ice Sheet at the Penultimate Glacial Maximum. Logarithmic scale bar for velocity fields shown by color scheme; contours on ice sheet are for surface elevation in meters. **e,** The Antarctic Ice Sheet at 116 ka. Logarithmic scale bar for velocity fields shown by color scheme; contours on ice sheet are for surface elevation in meters. **f,** Change in thickness of the Antarctic Ice Sheet between 116 ka and present day. Contours on ice surface and color scheme show change in thickness. **g,** Contributions of the Greenland and Antarctic Ice Sheets to global mean sea level between 140 ka and 116 ka.

Fig. 4. Predictions of relative sea level at four far-field sites. a, Relative sea-level (RSL) data from the Bahamas based on well-dated corals compared to a prediction of RSL using our simulated LIG loss from the Greenland and Antarctic Ice Sheets and the LAM ice history[22] (solid green line) and the HYB ice history (solid blue line) (see Methods). Also shown are predictions of RSL using just the LAM ice history[22] (dashed green line) and the HYB ice history (dashed blue line). **b, c,** As in **a**, except for Western Australia (**b)** and the Seychelles **(c)**. Uncertainties are for age (2σ), elevation (downward) and coral-depth habitat (upward). **d,** RSL data from Mallorca based on speleothem records. Uncertainties are for age (2σ) and growth. The Earth models used in the calculations are characterized by a lithospheric thickness, and upper and lower mantle viscosity

of: 140 km, 0.3 X 10^{21} Pas, 8.0 X 10^{22} Pa s (**a)**, 96 km, 0.3 X 10^{21} Pas, 5.0 X 10^{22} Pa s (**b)**, 30 km, 0.5 X 10^{21} Pas, 3.0 X 10^{22} Pa s (**c)**, and 120 km, 2.0 X 10^{21} Pas, 8.0 X 10^{22} Pa s (**d)**. Each of the coral records are comprised of data collected from multiple sites and the RSL predictions are shown for the following representative locations: 24.05°N, 285.47°E (**a)**, 21.97°S, 113.93°E (**b)**, 4.28°S, 55.73°E (**c)**, and 39.61°N, 3.38°E (**d)**. The consistency between the data and the predictions would be unaffected if we plotted RSL histories at each location that accounted for the variable collection sites.

Methods

Transient climate modeling. We use the fully-coupled configuration of the Community Climate System Model version 3 (CCSM3) in T31 resolution[30] for the transient simulation of the penultimate deglaciation and last interglaciation (LIG) from 140 to 120 ka. CCSM3 was used in the TraCE-21K transient simulation of the past 21,000 years spanning the last deglaciation and the current interglaciation[17,21,31]. The transient simulation of the penultimate deglaciation was initialized with a 600-year equilibrium simulation of the penultimate glacial maximum that branched off the TraCE-21K last glacial maximum (LGM) simulation with orbital configuration[7] and greenhouse gas contribution (CO_2) for 140 kyr[32]. The transient simulation of penultimate deglaciation with CCSM3 was integrated from 140 ka to 129 ka with changing atmospheric greenhouse gas concentrations[32], Earth's orbit[7], and continental ice sheets based on ICE-5G[33] but with the timing of the corresponding sea-level rise adjusted to closely follow the Waelbroeck et al.[1] and Grant et al.[34] sea-level reconstructions for the penultimate deglaciation (Extended Data Figs. 2, 3). We note that our sea-level modeling suggests that the sizes of the penultimate glacial maximum Northern Hemisphere ice sheets differed from the LGM and thus our climate modelling does no account for these important difference between the two terminations. Further climate modeling is thus needed to assess how these differences may have affected atmospheric circulation over the North Atlantic Ocean and the AMOC.

To simulate the impact of freshwater forcing from Heinrich event 11 on the Atlantic Meridional Overturning Circulation, freshwater is added at the surface of the North Atlantic in the area between 50°-70°N, being ramped to 0.17 Sverdrups (Sv; 10^6 m^3 s^{-1}) from 138 ka to 135.5 ka where it remains until 129.7 ka when it is shut off (Extended Data Fig. 3). The transient simulation of the LIG with CCSM3 was integrated from 129 ka to 116 ka with changing orbits and

atmospheric greenhouse gases under present-day ice-sheet configuration. No additional freshwater fluxes were applied during the transient simulation of the LIG.

Ice-sheet modeling. We use version 0.7.1 of the Parallel Ice Sheet Model (PISM), in which the dynamical core superposes velocity fields from the shallow shelf and shallow ice approximations across the entire domain. Fast flow ("streaming") of grounded ice is enabled by plastic failure of subglacial sediments, which depends on a prescribed but spatially-variable till friction angle, representing sediment strength and its degree of saturation. The till friction angle is based primarily on topography, so that deeper areas have lower friction angles. This mimics the effect of weaker sediments accumulating in deeper basins. The parameterization follows the form, *phi min / phi max / elevation min / elevation max*, in which the *phi min* is the friction angle applied below *elevation min*, *phi max* is the friction angle applied above *elevation max*, and values in between are linearly interpolated. For our Greenland simulations we prescribe values of 10 / 30 / -300 / 300, and for Antarctica 6 / 30 / -700 / -100. These values are based on, but modified from, previous work (Aschwanden et al.[35] for Greenland; Golledge et al.[36] for Antarctica), but these values are uncertain. Our values were chosen following exploratory simulations that sought to best capture the broad-scale geometric and dynamic features of the ice sheets.

Sediment strength evolves dynamically depending on the basal ice temperature. Where ice is sufficiently thick to allow basal melting, meltwater weakens the substrate until driving stresses exceed till cohesion. Failure of the substrate that results in acceleration of overlying ice follows a pseudo-plastic law[37,38], such that a small increase in stress above the shear strength of the substrate leads to an increasing velocity response. This ultimately thins the ice, which reduces the gravitational driving stress and results in a deceleration of the ice sheet. The cyclic behavior of ice streams that occurs as a consequence of this mechanism is described in more detail elsewhere[39].

PISM uses a sub-grid grounding line scheme[40] in which the interpolation of sub-ice shelf melt across the grounded to floating transition may be turned on or off. When turned on, the scheme tends to accelerate ice-sheet retreat in marine basins, whereas when it is off, the scheme produces a slower response[36]. This difference in behavior results in differences in retreat rates, but equilibrium states (for example, ice volume) are less affected. In our experiments we investigated both approaches, and found that interpolating sub-shelf melt across the grounding line produced simulations that were most closely in keeping with geological constraints for Termination I (T-I) (see below).

We also used a range of enhancement factors for the shallow ice (SIAe) and shallow shelf (SSAe) equations (SIAe = 1, 2, 3; SSAe = 0.5, 1), and different values for the basal sliding exponent that controls how plastic or linear the substrate deformation response to applied driving stresses (q = 0.25, 0.6). Floating ice is controlled by two calving mechanisms – one based on horizontal strain rates[41] and another that prescribes a minimum thickness criterion (50 m for Greenland, 200 m in Antarctica).

We run separate simulations for the Greenland and Antarctic ice sheets, both at 20-km resolution. To drive our ice-sheet model, we use output climatologies from the transient CCSM3 simulations described above for T-I and Termination II (T-II). Atmospheric outputs are applied as anomalies to present-day air temperature and precipitation fields[42,43], in the same manner as employed previously[44]. We employ a positive-degree day (PDD) model to translate temperatures above freezing into surface melt, of which 60% remains in the snowpack as a consequence of refreezing during percolation. The proportion of refreezing that takes place even under present conditions is difficult to constrain precisely[45] so we use a uniform value both for the control and perturbation experiments, in order to minimize the effects of this parameterization. That is,

differences in the simulation outputs are unlikely to arise from uncertainty in this aspect of model parameterization.

During our model tuning process, we explored a wide range of degree-day values (from 1 mm $^{o}C^{-1}$ day^{-1} up to 64 mm $^{o}C^{-1}$ day^{-1}) independently for both snow and ice. We tried the more usual melt threshold of 273 K and the lower value of 270 K following van den Broeke et al.[46]. The latter method yields more widespread melt, mimicking the possible melt arising from short-wave radiation under sub-freezing conditions, and thus degree-day factors are typically lower (van den Broeke et al., 2010). We also allow for stochastic variability in daily temperatures using a zero-mean white noise component whose standard deviation is set at 5 K. Although the choice of PDD parameters did exert some control on the geometry of the evolving ice mass, the basic shape of the ice sheet evolved in a similar manner regardless of either the melt forcing or the glaciological parameterization, suggesting that the dominant control on ice-sheet geometry is the climate forcing from the GCM. Recent work has shown that our simulations of surface mass balance (SMB) of the Greenland Ice Sheet under the high boreal summer insolation of the LIG may be sensitive to climate model resolution and SMB model type (i.e., PDD, surface energy balance)[47].

Oceanic fields for temperature and salinity at 500 m depth were used as inputs to a thermodynamic ocean model that calculates basal melt from salt and heat-flux gradients across the ice/ocean interface, according to the scheme described in[48]. As with the atmospheric variables, we apply the oceanic fields as anomalies from a present-day ocean configuration that for Antarctica is tuned to reproduce observed melt-rate patterns[49]. Since such constraints are not currently available for Greenland, we use a spatially uniform melt factor instead, which is iteratively refined so that both LGM and present-day ice-sheet extents are reproduced (see below). Ice thickness and bed topography for the two ice sheets are taken from the most recent compilations[50,51].

With the model set-up as described above, we ran a series of time-evolving experiments that first focused on T-I, rather than T-II. The rationale for this approach is that substantial geological data exist with which to constrain the evolving ice-sheet geometry through the last deglaciation, whereas there are few constraints for the preceding T-II. Therefore, in order to optimize our parameter settings, we undertook >500 experiments of T-I for both ice sheets until a good fit to empirical constraints was found. For Antarctica, our guiding constraints are that the ice sheet at the LGM, immediately prior to T-I, should occupy the majority of the continental shelf, and have an ice-volume excess above present that is within the range of 5.6-14.5 m represented by previous simulations[52-55]. Furthermore, we required that the evolution of the simulated ice sheet must reproduce the glacial maximum thickening of West Antarctica and thinning of East Antarctica inferred from ice-core analyses[55], and exhibit a pattern of mass loss that is consistent with geologically inferred deglacial changes in ice discharge[56]. In Greenland, geological constraints on the offshore extent of the LGM ice sheet are sparse, but the ice volume excess is thought to have been in the range 2 – 5 m global mean sea level equivalent[57,58]. We use this range as our target (Extended Data Fig. 8). Finally, both ice sheets are required to reproduce present-day grounded ice extent and volume as closely as possible at the end of the T-I simulations.

Once this phase of parameter optimization is complete, we run our experiments for T-II using the exact same settings, changing only the input climatology based on outputs from CCSM3. This dual approach allows for the robust simulation of a period, such as T-II, for which little data exist to constrain outputs. In addition, this methodology allows for the direct comparison of model outputs for the two periods, allowing any differences to be attributed solely to the imposed climate forcing rather than to uncertainties in the modelling procedure. Finally, by tuning the model to fit relatively well-known constraints such as LGM and present-day extent and volume, we reduce the

453 influence of any inaccuracies in the climate model representation of air or ocean temperatures
454 during the periods of simulation. Thus, if CCSM3 under- or overestimates the magnitude of past
455 climate anomalies with respect to present, the internal consistency between the T-I and T-II climate
456 simulations coupled with the data-constrained simulation of T-I mean that the reliability of the T-
457 II simulation is unaffected.

458 A novelty of our ice-sheet simulations compared to previous studies[59,60] is that we use a
459 fully evolving T-I experiment to constrain our model parameterizations. This includes components
460 such as degree-day factors for the PDD scheme. For Greenland, we run an ensemble of tuning
461 experiments that explore a range of snow and ice melt factors as well as ice-flow enhancement
462 coefficients (Extended Data Fig. 8). By then selecting the parameterization that at the end of the
463 T-I simulation most closely reproduces present-day ice volume and geometry we ensure that the
464 surface melt fields we generate are realistic. We then apply this setup to our T-II experiments. Our
465 annual temperature range is defined by the CCSM3 outputs. However, we also experimented with
466 duplicate simulations in which we modified our Greenland climatologies to incorporate summer
467 temperatures from Fausto et al.[42]. These simulations resulted in only minor differences in mass
468 change, suggesting that in our experiments, atmospheric forcing plays a lesser role than oceanic
469 forcing (Extended Data Figs. 6, 9). This is supported by experiments in which we also explored
470 alternative grounding line schemes to make the ice sheets either more or less sensitive to ocean
471 temperature change. In the less sensitive experiments, the ice sheet failed to advance sufficiently
472 far offshore, and was thus incompatible with geological constraints.

473 **Predictions of relative sea level.** Calculations of glacial isostatic adjustment described in the text
474 are based on a pseudo-spectral sea-level theory[23] for the case of spherically symmetric (i.e.,
475 rheology varies with depth alone), Maxwell viscoelastic Earth models, with a truncation at

476 spherical harmonic degree and order 256. The theory incorporates time-varying coastlines,
477 changes in the perimeter of grounded, marine-based ice sheets, and the impact on sea level of load-
478 induced perturbations to the Earth's rotation axis, where these perturbations are computed using
479 the rotational stability theory of Mitrovica et al.[61]. Profiles of the density and elastic structure of
480 the Earth model are taken from the seismic Preliminary Reference Earth Model[62]. The viscosity
481 structure of the Earth models is defined by three layers, a lithospheric zone of infinite viscosity,
482 and sub-lithospheric upper and lower mantle regions, where the boundary between the latter two
483 regions is taken to be 670 km depth. The thickness of the lithosphere and the viscosity of the upper
484 and lower mantle are free parameters of the modeling and are varied, respectively, within the
485 following ranges: 30 – 140 km; 2-20 X 10^{20} Pa s; and 2-100 X 10^{21} Pa s.

486 The set of five ice histories adopted in this study are based, in part, on histories constructed
487 by Dendy et al.[28] in their investigation of the sensitivity of LIG sea level predictions to variations
488 in the timing and geometry of ice cover during Marine Isotope Stage 6. We begin by summarizing
489 these ice histories.

490 All models in Dendy et al.[28] use the ICE6G ice history[63] for the period extending from the
491 LGM to present day and they extend back four full glacial cycles. The models are constrained to
492 have interglacial ice volumes and geometry identical to present-day ice cover on the Earth (i.e.,
493 there is no excess ice melting during previous interglaciations, including the LIG). The so-called
494 WAE ice model adopts the eustatic sea-level curve estimated by Waelbroeck et al.[1] on the basis of
495 benthic foraminifera isotope records. In the period prior to the LGM, the ice geometry is
496 constrained to be identical to the geometry post-LGM whenever the eustatic values are identical.
497 The LAM and COL models in Dendy et al.[28] also adopt the pre-LGM eustatic curve of Waelbroeck
498 et al.[1], but are distinguished from WAE by their ice history during the penultimate glacial cycle.

499 In particular, these models adopt the ice geometry during the penultimate glacial maximum (PGM)
500 inferred by Lambeck et al.[22] and Colleoni et al.[27], which are both characterized by more significant
501 ice cover over Eurasia during the PGM than the LGM. Since the difference in peak Eurasian ice
502 volume during the PGM in the LAM and COL models is large (55 m and 71 m, respectively, in
503 units of equivalent GMSL), we have constructed an intermediate ice history (HYB) that is
504 essentially the average of these models (peak volume of 66 m GMSL equivalent during the PGM)
505 The increased ice cover of the LAM, HYB and COL models relative to the WAE model is
506 compensated, in large part, by a reduction of the volume of the Laurentide Ice Sheet during the
507 PGM relative to the LGM[22,27]. All four models, WAE, LAM, HYB and COL, converge to the same
508 ice geometry (i.e., the present-day ice geometry) at the beginning of the model LIG. We note that
509 we have adapted the WAE, LAM and COL models described by Dendy et al.[28] to more closely
510 follow the eustatic curve of Waelbroeck et al.[1]. Finally, the model SHA in Dendy et al.[28] is
511 constructed in a manner identical to WAE, with the exception that the model adopts the eustatic
512 curve derived by Shakun et al.[64] in the period prior to the LGM.

513 The ice histories considered in the present study combine the five models described above
514 with the Antarctic and Greenland Ice Sheet histories discussed in the main text. Specifically, the
515 difference in ice height during the period from 140 ka to 116 ka relative to the present day in the
516 ice-sheet simulations of the main text are applied to each of the Dendy et al.[28] models. The net
517 result is that the five models constructed in this manner are characterized, in contrast to those in
518 Dendy et al.[28], with excess melting of the Antarctic and Greenland Ice Sheets during the LIG
519 relative to present-day. We ran 337 Earth models for each of the five ice histories (total of 1685
520 simulations) in which parameters defining the Earth model were varied over plausible ranges.

In exploring the fit of the relative sea level (RSL) predictions to the coral record, we considered three sites that have the largest data sets of well-dated corals (Bahamas, Seychelles and Western Australia) and a relatively new speleothem data set from Mallorca (*43*) (Extended Data Fig. 7). Given that corals provide a minimum bound on sea level, our metric for fit for these data was the number of coral records that any specific RSL prediction bounded from above. In contrast, we interpret the height uncertainties associated with the published speleothem data to represent a two-way bound on peak RSL.

None of the 1685 simulations (i.e., our sampling of 337 Earth models and 5 ice histories) were successful in bounding all coral records from above. As an indication of performance, Extended Data Fig. 7 shows predictions from the full suite of simulations that satisfy the following criteria: (1) all coral data from Western Australia and Bahamas, with the exception of the earliest datum at the latter site (at ~131 ka), fall below the prediction; and (2) the prediction at the Seychelles falls above all three coral records at an elevation of ~4 m. The various lines on the figure represent the different Earth models for each ice history that satisfy these constraints. For each ice history (i.e., each column of Extended Data Fig. 7), the Earth models sampled on each frame (i.e., each site) represent a discrete set that may or may not overlap with the set from a different site. As an example, in the case of the LAM and COL ice histories, no single Earth model appears on the results for all three sites. This is reflected in Fig. 4 in the main text, where the simulation highlighted in each frame is the result for a distinct Earth model. This variation is justified by the fact that the Earth's mantle is subject to large amplitude variations in viscoelastic structure and so it would be unexpected if the sea-level response at each of the three sites preferred the same Earth model.

543 Note that the number of simulations that satisfy our plotting criterion for the Bahamas
544 increases as one moves to ice histories with larger Eurasian ice cover at the PGM (i.e., from the
545 WAE to the COL results), but the number of simulations that satisfy the criteria for the Seychelles
546 decreases in the same sense. While not apparent from Extended Data Fig. 7, the predicted
547 highstand at Seychelles increases as one considers Earth models with progressively thinner elastic
548 lithospheres (see Ref. 28, Fig. 9A), and the simulations that predict RSL highstands above the
549 Seychelles records are those based on a lithospheric thickness of 30 km (as in Fig. 4 of the main
550 text) or, in a couple of cases for the WAE ice history, 50 km. This raises two important issues.
551 First, none of the simulations that yield RSL above all the coral elevations at Seychelles also satisfy
552 the geological constraints at the Bahamas. Second, since the predicted highstand at the Seychelles
553 is sensitive to the adopted lithospheric thickness, there is a trade-off between the preferred value
554 of this parameter and the level of excess melting during the LIG. That is, increasing polar ice sheet
555 melting above the ~4 m GMSL equivalent adopted in the simulations in Extended Data Fig. 7,
556 would increase the range of lithospheric thickness that would satisfy the Seychelles coral record,
557 and thus bring the inference into better accord with other GIA-based estimates of this Earth model
558 parameter.

559 This issue may also have relevance in regard to the results for Mallorca (Extended Data
560 Fig. 7) where simulations are only plotted if the misfit between the GIA predictions and the
561 speleothem observations is within 50% of the minimum misfit achieved in all simulations. In this
562 case, fewer of the simulations provide a reasonable fit to the speleothem record as one considers
563 ice histories with progressively larger volumes over Eurasia at PGM and, indeed, no simulations
564 based on the COL ice history satisfy our plotting criterion. However, regardless of the adopted ice
565 history, none of the simulations fit the highstand constraints before 125 ka. Bringing the GIA

566 predictions in Extended Data Fig. 7 into accord with the Mallorca observations would require
567 additional excess melting that is limited to the earliest phase of the LIG.

568 As a final point, simulations based on the SHA ice history yielded misfits significantly
569 larger than predictions shown in Extended Data Fig. 7.

570 The sea-level simulations described above yield changes in sea level and topography at
571 each time slice of the ice history. As an example, Extended Data Fig. 5 shows the reconstructed
572 topography for the area covered by the Scandinavian Ice Sheet at 131 ka, near the end of the MIS6
573 deglaciation, for a simulation based on the LAM ice history and a specific Earth model (see
574 caption). The map supports the suggestion in the main text that the margin of grounded ice
575 complexes in this region across MIS 6 through 5e were marine based.

576 **Evidence for warming over the Greenland Ice Sheet during the Last Interglaciation.** Here we
577 evaluate the evidence for warming over the Greenland Ice Sheet during the Last Interglaciation
578 (LIG). This supports our climate model simulation that while the LIG atmosphere was warmer
579 than pre-Industrial, it largely remained below freezing and did not lead to significant mass loss
580 from surface melting.

581 Regarding the reconstructed LIG temperatures at the NEEM[65] and GISP2[66] ice-core sites,
582 there is uncertainty in which $d\delta^{18}O_{ice}/dT$ relationship should be used to reconstruct LIG
583 temperatures, and this uncertainty is exacerbated when applying the modern $d\delta^{18}O_{ice}$-dT
584 relationship to past climates, where differences in orbital forcing, moisture transport pathways,
585 ice-sheet topography, and sea-ice extent can change the relationship[67-72]. To illustrate some of
586 these uncertainties, we have compared our simulated temperatures for the NEEM and GISP2 ice-
587 core sites with the temperature reconstructions for these sites based on $\delta^{18}O_{ice}$ (Extended Data Fig.
588 10). These reconstructions span the interval 127-120 ka, which is the warmest interval in the ice-

589 core records for the LIG suggested by this proxy. The published reconstructed temperatures for
590 GISP2 (blue symbols on upper panel)[66,73] and NEEM (dark blue line on lower panel)[65] are based
591 on the relation $d\delta^{18}O_{ice}/dT$ = ~0.5‰ C^{-1} which is derived from Greenland ice-core sites
592 elsewhere[74]. During the LIG, the precipitation-weighted $\delta^{18}O$ is likely biased to summer months
593 rather than mean annual temperature (van de Berg et al., 2013), so we compare this reconstruction
594 with our simulated summer temperature (JJA) (grey line on each panel). This suggests that our
595 simulated JJA temperatures are underestimating the mean of the reconstructions by 4-5ºC. This
596 difference is reduced when we account for our simulated ice-surface lowering of ~200 m at NEEM
597 and ~400 m at GISP2 (see Fig. 3C) and assume the lapse rate of 7.5ºC km^{-1} used by Dahl-Jensen
598 et al.[65], thus placing our results within the published uncertainties of the reconstructions (green
599 line on each panel).

600 However, following the publication of Dahl-Jensen et al.[65], Masson-Delmotte et al.[75]
601 established that the $d\delta^{18}O_{ice}/dT$ relation at the NEEM site is ~1.1‰ C^{-1}, suggesting that the NEEM
602 and GISP2 LIG summer temperatures are about half of the originally published values based on
603 the Vinther et al.[74] $d\delta^{18}O_{ice}/dT$ relation (red symbols on upper panel, red line on lower panel).
604 Masson-Delmotte et al.[75] (p. 1500) conclude that "For the last interglacial period, the observed
605 $\delta^{18}O$ anomaly of 3.6‰ at NEEM deposition site would then translate into 3.6$\pm$0.7 ºC warming,
606 instead of the estimate of 7.5$\pm$1.8 ºC (NEEM, 2013) that was obtained using the Greenland average
607 Holocene isotope–temperature relationship (Vinther et al., 2009)."

608 Our simulated JJA temperatures (grey line on each panel) are thus only 1-2ºC colder than
609 the mean reconstructions for GISP2 and NEEM based on this new calibration, but they are in
610 excellent agreement with the mean values when accounting for our modeled ice-surface lowering
611 (green line on each panel).

612 Landais et al.[76] used $\delta^{15}N$ from the NEEM core to reconstruct temperatures that were 8.5°
613 $\pm$ 2.5 °C warmer during the LIG compared to preindustrial (PI). However, the $\delta^{15}N$ reconstruction
614 represents annual temperature whereas the $\delta^{18}O_{ice}$ temperatures are biased to the summer, which
615 is the critical season for influencing changes in surface mass balance through melting. The two
616 temperature reconstructions are thus not directly comparable. Moreover, Landais et al.[76] identify
617 "large uncertainties" (p. 1944) in their temperature reconstruction, including in the firn model
618 used, in the assumed accumulation rates, and in the potential influence of surface melt on firn
619 depth.

620 We thus conclude that when using the most suitable temperature calibration for the ice-
621 core sites and within the uncertainties of the ice-core proxy reconstructions, our climate model
622 successfully captures the LIG summer (JJA) temperature anomaly relative to pre-Industrial at
623 NEEM and GISP2. Consistent with this model-data agreement for warmer LIG JJA temperatures,
624 we find that the LIG surface mass balance of the GrIS is more negative than present day (Extended
625 Data Fig. 9).

626 Dahl-Jensen et al.[65] stated "during our NEEM field campaigns (2007-2012), the mean
627 surface air temperature in July reached -5.4°C." However, Box[77] reported the average JJA
628 temperature for 2007-2012 at NEEM site as -10.9 $\pm$ 0.3°C, suggesting that Dahl-Jensen et al.[65] are
629 reporting a maximum July temperature value during their period of record rather than climatology.
630 But the JJA temperature that matters for comparing to the LIG is the pre-Industrial, which Box[77]
631 found to be -12.6 $\pm$ 0.6°C for 1840-1870 (period of record closest to pre-Industrial). (Dahl-Jensen
632 et al.[65] compared to the average of the last millennium.) Thus, even if the Dahl-Jensen et al.[65] LIG
633 temperature reconstruction is correct (7.5$\pm$1.8 °C warmer than the mean of the past millennium),
634 average LIG summer temperatures would still be well below freezing (~ -5°C). More likely,

635 however, they are even further below freezing when using the $d\delta^{18}O_{ice}/dT$ relation established for
636 the NEEM site[75], i.e., 3.6±0.7 ºC warmer than the mean of the past millennium, with average LIG
637 summer temperatures thus being -9ºC.

638 The evidence for surface melt at the NEEM ice core site is based on: (1) a low-resolution
639 record showing that out of 73 samples, seven have elevated CH_4 and N_2O during the interval 118-
640 127 ka, and (2) a high-resolution CH_4 record that suggests five melt events in the 123.5-122.5 ka
641 interval, or one every 200 years[65,78]. Noble gases that were measured at the times of four of the
642 five elevated CH_4 events in the high-resolution record confirm melting at these times[78]. This alone
643 makes it clear that these were infrequent periods of melting rather than continuous melting
644 throughout the LIG. According to Anais Orsi (personal communication, March, 2019), during a
645 melt event, such as the 2012 event[79], the melt percolates and refreezes in the top 1m of the firn,
646 often in many layers, so one melt event may be represented by more than one melt layer. Moreover,
647 although the noble gas results clearly identify four periods of enhanced melting, one cannot
648 exclude the possibility that each sample represents a single 2012-like melt event.

649 In summary, ice-core proxies suggest that Greenland LIG temperatures were warmer than
650 present, but constraining the amount of warming from these proxies remains uncertain. However,
651 even the highest estimates of warming still suggest that average JJA temperatures remained well
652 below freezing relative to pre-Industrial, and based on the more-appropriate $\delta^{18}O_{ice}$-temperature
653 calibration from Masson-Delmotte et al.[75], are in good agreement with our simulated temperatures
654 for the ice-core sites. Consistent with this model-data agreement for warmer LIG JJA temperatures,
655 we find that the LIG surface mass balance of the GrIS is more negative then present day. Rare
656 episodes of melting occurred, but while their frequency may increase under higher mean
657 temperatures and insolation, such as is recorded in the Holocene section of the GISP2 ice core[80],

658 we conclude that with a frequency of perhaps only one melt event every 200 years, they had a
659 negligible influence on long-term surface mass balance, and average summer temperatures at the
660 NEEM site otherwise remained well below freezing during the LIG.

661 **Influence of freshwater forcing from modeled mass loss from the Greenland and Antarctic**
662 **Ice Sheets on ocean circulation during the last interglaciation.** We did not include additional
663 freshwater (FW) forcing after 129.5 ka, but we show here that the FW fluxes from our modeled
664 mass loss from the Greenland and Antarctic ice sheets (GrIS and AIS) after 129.5 ka (during the
665 LIG) were too small to have influenced the Atlantic Meridional Overturning Circulation (AMOC)
666 or Antarctic Bottom Water (AABW) formation. Since global sea level reached modern at 129-130
667 ka, and our modeled AMOC resumes at 129.5 ka, we only consider the FW fluxes from the GrIS
668 and AIS since 129.5 ka.

669 From 129.5 to 127 ka, modeled GrIS mass loss was 0.2 m of sea-level equivalent, which
670 is equivalent to a FW flux of 0.0009 Sv. From 127 ka to 117.5 ka, GrIS mass loss was 0.09 m,
671 which is equivalent to 0.0001 Sv. For reference, Bakker et al.[81] showed that a FW flux of 0.01 Sv
672 from Greenland for the RCP4.5 scenario (see their Fig. SI3) results in a median reduction in the
673 AMOC of ~5% (their Fig. 2, GrIS only). The FW fluxes from LIG loss of the GrIS in our model
674 are two orders of magnitude smaller than this, and thus would have no impact on the AMOC, and
675 thus on our ice-sheet model simulations.

676 From 129.5ka to 123.5 ka, AIS mass loss was 4.1 m, which is equivalent to a FW flux of
677 0.008 Sv. Bakker et al.[82] found that a FW flux of 0.12 Sv from the AIS increases variability in
678 AABW by ~10% and in AMOC by ~5%. The FW fluxes from LIG loss of the AIS in our model
679 is a factor of 15 smaller than this, and thus would have no impact on AABW or the AMOC, and
680 thus on our ice-sheet model simulations.

Code availability.

CCSM3 is freely available as open-source code from http://www.cesm.ucar.edu/models/ccsm3.0/

PISM is freely available as open-source code from https://github.com/pism/pism.git.

Data availability

Antarctic bedrock topography and ice thickness data are from the BEDMAP2 compilation, available at https://secure.antarctica.ac.uk/data/bedmap2/. Greenland topography and ice thickness data are from BedMachine v3, available at https://nsidc.org/data/idbmg4. Greenland mass balance and geothermal heat flux data are available from the seaRISE website: http://websrv.cs.umt.edu/isis/index.php/Data. Information on Antarctic surface mass balance data are available at http://www.projects.science.uu.nl/iceclimate/models/antarctica.php#racmo23. Antarctic geothermal heat flux data are available at the Open Science Framework https://doi.pangaea.de/10.1594/PANGAEA.882503. The datasets generated and used for this study (Figs. 1,2,3,4, Extended Data Figs. 3,4,5,6,7,8,9) are available from the Open Science Framework (DOI 10.17605/OSF.IO/FX7WK).

30 Yeager, S. G., Shields, C. A., Large, W. G. & Hack, J. J. The low-resolution CCSM3. *Journal of Climate* **19**, 2545-2566, doi:10.1175/Jcli3744.1 (2006).

31 He, F. *Simulating transient climate evolution of the last deglaciation with CCSM3* Ph.D. thesis, The University of Wisconsin - Madison, (2011).

32 Luthi, D. *et al.* High-resolution carbon dioxide concentration record 650,000-800,000 years before present. *Nature* **453**, 379-382, doi:10.1038/nature06949 (2008).

33 Peltier, W. R. Global glacial isostasy and the surface of the ice-age earth: The ice-5G (VM2) model and grace. *Annual Review of Earth and Planetary Sciences* **32**, 111-149 (2004).

34 Grant, K. M. *et al.* Rapid coupling between ice volume and polar temperature over the past 150,000 years. *Nature* **491**, 744-747, doi:10.1038/nature11593 (2012).

35 Aschwanden, A., Fahnestock, M. A. & Truffer, M. Complex greenland outlet glacier flow captured. *Nature Communications* **7**, doi:10.1038/ncomms10524 (2016).

36 Golledge, N. R. *et al.* The multi-millennial Antarctic commitment to future sea-level rise. *Nature* **526**, 421-+, doi:10.1038/nature15706 (2015).

37 Schoof, C. A variational approach to ice stream flow. *Journal of Fluid Mechanics* **556**, 227-251, doi:Doi 10.1017/S0022112006009591 (2006).

38 Bueler, E. & Brown, J. Shallow shelf approximation as a "sliding law" in a thermomechanically coupled ice sheet model. *Journal of Geophysical Research-Earth Surface* **114**, F03008 (2009).

39 Van Pelt, W. J. J. & Oerlemans, J. Numerical simulations of cyclic behaviour in the Parallel Ice Sheet Model (PISM). *Journal of Glaciology* **58**, 347-360, doi:10.3189/2012JoG11J217 (2012).

40 Feldmann, J., Albrecht, T., Khroulev, C., Pattyn, F. & Levermann, A. Resolution-dependent performance of grounding line motion in a shallow model compared with a full-Stokes model according to the MISMIP3d intercomparison. *Journal of Glaciology* **60**, 353-360, doi:10.3189/2014JoG13J093 (2014).

41 Levermann, A. *et al.* Kinematic first-order calving law implies potential for abrupt ice-shelf retreat. *Cryosphere* **6**, 273-286, doi:10.5194/tc-6-273-2012 (2012).

42 Fausto, R. S., Ahlstrom, A. P., Van As, D., Boggild, C. E. & Johnsen, S. J. A new present-day temperature parameterization for Greenland. *Journal of Glaciology* **55**, 95-105, doi:Doi 10.3189/002214309788608985 (2009).

43 van Wessem, J. M. *et al.* Improved representation of East Antarctic surface mass balance in a regional atmospheric climate model. *Journal of Glaciology* **60**, 761-770, doi:10.3189/2014JoG14J051 (2014).

44 Golledge, N. R. *et al.* Antarctic climate and ice-sheet configuration during the early Pliocene interglacial at 4.23 Ma. *Climate of the Past* **13**, 959-975, doi:10.5194/cp-13-959-2017 (2017).

45 Munneke, P. K. *et al.* A new albedo parameterization for use in climate models over the Antarctic ice sheet. *Journal of Geophysical Research-Atmospheres* **116**, doi:10.1029/2010jd015113 (2011).

46 van den Broeke, M., C. Bus, C., Ettema, J. & P. Smeets, P. Temperature thresholds for degree-day modelling of Greenland ice sheet melt rates. *Geophysical Research Letters* **37**, L18501, doi:10.1029/2010GL044123 (2010).

47 Plach, A. *et al.* Eemian Greenland SMB strongly sensitive to model choice. *Climate of the Past* **14**, 1463-1485, doi:10.5194/cp-14-1463-2018 (2018).

48 Hellmer, H. H. & Olbers, D. J. A 2-Dimensional Model for the Thermohaline Circulation under an Ice Shelf. *Antarctic Science* **1**, 325-336 (1989).

49 Bernales, J., Rogozhina, I. & Thomas, M. Melting and freezing under Antarctic ice shelves from a combination of ice-sheet modelling and observations. *Journal of Glaciology* **63**, 731-744, doi:10.1017/jog.2017.42 (2017).

50 Morlighem, M. *et al.* BedMachine v3: Complete Bed Topography and Ocean Bathymetry Mapping of Greenland From Multibeam Echo Sounding Combined With Mass Conservation. *Geophysical Research Letters* **44**, 11051-11061, doi:10.1002/2017gl074954 (2017).

51 Fretwell, P. *et al.* Bedmap2: improved ice bed, surface and thickness datasets for Antarctica. *Cryosphere* **7**, 375-393, doi:10.5194/tc-7-375-2013 (2013).

52 Mackintosh, A. *et al.* Retreat of the East Antarctic ice sheet during the last glacial termination. *Nature Geoscience* **4**, 195-202, doi:10.1038/NGEO1061 (2011).

53 Briggs, R., Pollard, D. & Tarasov, L. A glacial systems model configured for large ensemble analysis of Antarctic deglaciation. *Cryosphere* **7**, 1949-1970, doi:10.5194/tc-7-1949-2013 (2013).

54 Golledge, N. R., Fogwill, C. J., Mackintosh, A. N. & Buckley, K. M. Dynamics of the last glacial maximum Antarctic ice-sheet and its response to ocean forcing. *Proceedings of the National Academy of Sciences of the United States of America* **109**, 16052-16056, doi:10.1073/pnas.1205385109 (2012).

55 Golledge, N. R. *et al.* Antarctic contribution to meltwater pulse 1A from reduced Southern Ocean overturning. *Nature Communications* **5** (2014).

56 Weber, M. E. *et al.* Millennial-scale variability in Antarctic ice-sheet discharge during the last deglaciation. *Nature* **510**, 134-+, doi:Doi 10.1038/Nature13397 (2014).

57 Simpson, M. J. R., Milne, G. A., Huybrechts, P. & Long, A. J. Calibrating a glaciological model of the Greenland ice sheet from the Last Glacial Maximum to present-day using field observations of relative sea level and ice extent. *Quaternary Science Reviews* **28**, 1631-1657, doi:10.1016/j.quascirev.2009.03.004 (2009).

58 Lecavalier, B. S. *et al.* A model of Greenland ice sheet deglaciation constrained by observations of relative sea level and ice extent. *Quaternary Science Reviews* **102**, 54-84, doi:Doi 10.1016/J.Quascirev.2014.07.018 (2014).

59 Stone, E. J., Lunt, D. J., Annan, J. D. & Hargreaves, J. C. Quantification of the Greenland ice sheet contribution to Last Interglacial sea level rise. *Climate of the Past* **9**, 621-639, doi:10.5194/cp-9-621-2013 (2013).

60 Goelzer, H., Huybrechts, P., Loutre, M. F. & Fichefet, T. Last Interglacial climate and sea-level evolution from a coupled ice sheet-climate model. *Climate of the Past* **12**, 2195-2213, doi:10.5194/cp-12-2195-2016 (2016).

61 Mitrovica, J. X., Wahr, J., Matsuyama, I. & Paulson, A. The rotational stability of an ice-age earth. *Geophysical Journal International* **161**, 491-506 (2005).

62 Dziewonski, A. M. & Anderson, D. L. Preliminary reference Earth model. *Physics of the Earth and Planetary Interiors* **25**, 297-356 (1981).

63 Peltier, W. R., Argus, D. F. & Drummond, R. Space geodesy constrains ice age terminal deglaciation: The global ICE-6G_C (VM5a) model. *Journal of Geophysical Research-Solid Earth* **120**, 450-487, doi:10.1002/2014jb011176 (2015).

64 Shakun, J. D., Lea, D. W., Lisiecki, L. E. & Raymo, M. E. An 800-kyr record of global surface ocean delta O-18 and implications for ice volume-temperature coupling. *Earth and Planetary Science Letters* **426**, 58-68, doi:10.1016/j.epsl.2015.05.042 (2015).

65 Dahl-Jensen, D. *et al.* Eemian interglacial reconstructed from a Greenland folded ice core. *Nature* **493**, 489-494 (2013).

66 Yau, A., Bender, M. L., Robinson, A. & Brook, E. J. Reconstructing the last interglacial at Summit, Greenland: Insights from GISP2. *Proceedings of the National Academy of Sciences* **113**, 9710-9715, doi:10.1073/pnas.1524766113 (2016).

67 Liu, Z. Y. *et al.* Younger Dryas cooling and the Greenland climate response to CO2. *Proceedings of the National Academy of Sciences of the United States of America* **109**, 11101-11104, doi:10.1073/pnas.1202183109 (2012).

68 van de Berg, W. J., van den Broeke, M. R., van Meijgaard, E. & Kaspar, F. Importance of precipitation seasonality for the interpretation of Eemian ice core isotope records from Greenland. *Climate of the Past* **9**, 1589-1600, doi:10.5194/cp-9-1589-2013 (2013).

69 Sime, L. C. *et al.* Warm climate isotopic simulations: what do we learn about interglacial signals in Greenland ice cores? *Quaternary Science Reviews* **67**, 59-80, doi:10.1016/j.quascirev.2013.01.009 (2013).
70 Buizert, C. *et al.* Greenland temperature response to climate forcing during the last deglaciation. *Science* **345**, 1177-1180, doi:10.1126/science.1254961 (2014).
71 Rhines, A. & Huybers, P. J. Sea Ice and Dynamical Controls on Preindustrial and Last Glacial Maximum Accumulation in Central Greenland. *Journal of Climate* **27**, 8902-8917, doi:10.1175/JCLI-D-14-00075.1 (2014).
72 Pedersen, R. A., Langen, P. L. & Vinther, B. M. Greenland during the last interglacial: the relative importance of insolation and oceanic changes. *Climate of the Past* **12**, 1907-1918, doi:10.5194/cp-12-1907-2016 (2016).
73 Suwa, M., von Fischer, J. C., Bender, M. L., Landais, A. & Brook, E. J. Chronology reconstruction for the disturbed bottom section of the GISP2 and the GRIP ice cores: Implications for Termination II in Greenland. *Journal of Geophysical Research-Atmospheres* **111**, -, doi:10.1029/2005jd006032 (2006).
74 Vinther, B. M. *et al.* Holocene thinning of the Greenland ice sheet. *Nature* **461**, 385-388, doi:10.1038/nature08355 (2009).
75 Masson-Delmotte, V. *et al.* Recent changes in north-west Greenland climate documented by NEEM shallow ice core data and simulations, and implications for past-temperature reconstructions. *The Cryosphere* **9**, 1481-1504 (2015).
76 Landais, A. *et al.* How warm was Greenland during the last interglacial period? *Climate of the Past* **12**, 1933-1948, doi:10.5194/cp-12-1933-2016 (2016).
77 Box, J. E. Greenland Ice Sheet Mass Balance Reconstruction. Part II: Surface Mass Balance (1840-2010). *Journal of Climate* **26**, 6974-6989, doi:10.1175/JCLI-D-12-00518.1 (2013).
78 Orsi, A. J. *et al.* Differentiating bubble-free layers from melt layers in ice cores using noble gases. *Journal of Glaciology* **61**, 585-594, doi:10.3189/2015JoG14J237 (2015).
79 Tedesco, M. *et al.* Evidence and analysis of 2012 Greenland records from spaceborne observations, a regional climate model and reanalysis data. *Cryosphere* **7**, 615-630, doi:10.5194/tc-7-615-2013 (2013).
80 Alley, R. B. & Anandakrishnan, A. Variations in melt-layer frequency in the GISP2 ice core: implications for Holocene summer temperatures in central Greenland. *Annals of Glaciology* **21**, 64-70 (1995).
81 Bakker, P. *et al.* Fate of the Atlantic Meridional Overturning Circulation: Strong decline under continued warming and Greenland melting. *Geophysical Research Letters* **43**, 12252-12260, doi:10.1002/2016GL070457 (2016).
82 Bakker, P., Clark, P. U., Golledge, N. R., Schmittner, A. & Weber, M. E. Centennial-scale Holocene climate variations amplified by Antarctic Ice Sheet discharge. *Nature* **541**, 72-+, doi:10.1038/nature20582 (2017).
83 Deaney, E. L., Barker, S. & van de Flierdt, T. Timing and nature of AMOC recovery across Termination 2 and magnitude of deglacial CO2 change. *Nature Communications* **8**, doi:10.1038/ncomms14595 (2017).
84 Bazin, L. *et al.* An optimized multi-proxy, multi-site Antarctic ice and gas orbital chronology (AICC2012): 120-800 ka. *Climate of the Past* **9**, 1715-1731, doi:10.5194/cp-9-1715-2013 (2013).

85 Oppo, D. W., McManus, J. F. & Cullen, J. L. Evolution and demise of the Last Interglacial warmth in the subpolar North Atlantic. *Quaternary Science Reviews* **25**, 3268-3277, doi:10.1016/j.quascirev.2006.07.006 (2006).

86 Skinner, L. C. & Shackleton, N. J. Deconstructing Terminations I and II: revisiting the glacioeustatic paradigm based on deep-water temperature estimates. *Quaternary Science Reviews* **25**, 3312-3321, doi:10.1016/j.quascirev.2006.07.005 (2006).

87 Goni, M. F. S. *et al.* European climate optimum and enhanced Greenland melt during the Last Interglacial. *Geology* **40**, 627-630, doi:10.1130/G32908.1 (2012).

88 Roberts, N. L., Piotrowski, A. M., McManus, J. F. & Keigwin, L. D. Synchronous deglacial overturning and water mass source changes. *Science* **327**, 75-78, doi:10.1126/science.1178068 (2010).

89 McManus, J. F., Francois, R., Gherardi, J. M., Keigwin, L. D. & Brown-Leger, S. Collapse and rapid resumption of Atlantic meridional circulation linked to deglacial climate changes. *Nature* **428**, 834-837, doi:10.1038/nature02494 (2004).

90 Stern, J. V. & Lisiecki, L. E. North Atlantic circulation and reservoir age changes over the past 41,000years. *Geophysical Research Letters* **40**, 3693-3697, doi:10.1002/grl.50679 (2013).

91 Menviel, L. *et al.* The penultimate deglaciation: protocol for PMIP4 transient numerical simulations between 140 and 127 ka. *Climate of the Past Discussions*, doi:doi.org/10.5194/cp-2018-106 (2018).

92 Thomas, A. L. *et al.* Penultimate Deglacial Sea-Level Timing from Uranium/Thorium Dating of Tahitian Corals. *Science* **324**, 1186-1189, doi:10.1126/science.1168754 (2009).

93 Esat, T. M., McCulloch, M. T., Chappell, J., Pillans, B. & Omura, A. Rapid fluctuations in sea level recorded at Huon Peninsula during the penultimate deglaciation. *Science* **283**, 197-201, doi:DOI 10.1126/science.283.5399.197 (1999).

94 Cheng, H. *et al.* Improvements in Th-230 dating, Th-230 and U-234 half-life values, and U-Th isotopic measurements by multi-collector inductively coupled plasma mass spectrometry. *Earth and Planetary Science Letters* **371**, 82-91, doi:10.1016/j.epsl.2013.04.006 (2013).

95 Peak, B. A., Mitrovica, J. X., Latychev, K., Powell, E. & Lau, H. C. P. Complex earth structure and glacial isostatic adjustment in the Red Sea. *American Geophysical Union*, PP13C-1343 (2018).

96 Lambeck, K. *et al.* Sea level and shoreline reconstructions for the Red Sea: isostatic and tectonic considerations and implications for hominin migration out of Africa. *Quaternary Science Reviews* **30**, 3542-3574 (2011).

97 Lambeck, K., Rouby, H., Purcell, A., Sun, Y. & Sambridge, M. Sea level and global ice volumes from the Last Glacial Maximum to the Holocene. *Proceedings of the National Academy of Sciences* **111**, 15296-15303 (2014).

888 **Extended Data Fig. 1. Climate and sea-level records for Termination II and Termination I.**
889 **(a)** εNd records from the North Atlantic Ocean as proxies of Atlantic meridional overturning
890 circulation (AMOC)[16,83]. **(b)** CCSM3 maximum AMOC transport (below 500 m) (this study). **(c)**
891 EPICA Dome C δD record on AICC2012 age model as proxy of Antarctic temperature[84] (blue
892 line) and percentage of warm planktonic foraminiferal species as proxy of North Atlantic sea
893 surface temperatures[83] (grey line). **(d)** $\delta^{18}O$ record from Chinese stalagmite as proxy of Asian
894 monsoon strength[18]. **(e)** Rate of sea-level change derived from a relative sea level (RSL)
895 reconstruction based on benthic foraminifera isotopes[1]. **(f)** A stack of North Atlantic ice-rafted
896 debris records recording Heinrich event 11 (H11)[83,85-87]. **(g)** εNd[88] (brown, orange symbols) and
897 Pa/Th[89] (purple, green symbols, 1 sigma uncertainty) records from the North Atlantic Ocean as
898 proxies of AMOC. **(h)** CCSM3 maximum AMOC transport (below 500 m) (this study). **(i)** EPICA
899 Dome C δD record on AICC2012 age model (dark blue line)[84] as proxy of Antarctic temperature
900 and temperature reconstruction from the Greenland GISP2 ice core (light blue line)[70]. **(j)** $\delta^{18}O$
901 record from Chinese stalagmite as proxy of Asian monsoon strength[18]. **(k)** Rate of sea-level change
902 derived from a RSL reconstruction based on benthic foraminifera isotopes[1]. **(l)** A stack of North
903 Atlantic ice-rafted debris records recording Heinrich event 1 (H1)[90].
904
905 **Extended Data Fig. 2. Sea-level records for the last two terminations and interglaciations. (a)**
906 Sea-level reconstructions for the penultimate deglaciation and the last interglaciation (the latter
907 identified by the grey-shaded area). Eustatic sea-level record is based on benthic foraminifera
908 isotopes (blue line with 1σ uncertainty)[1] and relative sea-level (RSL) record is based on Red Sea
909 isotopes (gray crosses; green line, 1-kyr moving Gaussian filter)[34] placed on a revised age model[91].
910 Also shown are RSL data from U-series dated corals at Tahiti (sky blue circles)[92], Huon Peninsula

(light blue green circle; altered samples shown by gray circles)[93], the Seychelles (light green circles)[25], western Australia (blue circles)[24], and the Bahamas (cyan circles)[24]. All of the U-series ages have been recalculated to normalize them with the same set of decay constants for ^{234}U and ^{230}Th[94] and are shown with 2σ age uncertainty. We note that the offset between the Red Sea record (green line) and the benthic foraminifera record (blue line) may reflect the complex 3-dimensional Earth structure in the vicinity of the Red Sea rift[95,96]. The variability in the Red Sea and Huon Peninsula RSL records may reflect a sea-level reversal at ~137 ka[91] which, if it existed, was too small to be recorded by the benthic foraminiferal record. The rate of sea-level change based on the benthic foraminiferal record is also shown. **(b)** Sea-level reconstructions for the last deglaciation and the present interglaciation (the latter identified by the grey-shaded area). The record of global mean sea level is based on benthic foraminifera isotopes (blue line with 1σ uncertainty)[1]. Also shown are individual sea-level estimates (black circles, 2σ uncertainty) that have been corrected for glacial isostatic adjustment[97]. Rate of sea-level change based on the benthic foraminiferal record is also shown. **(c)** Upper panel shows eustatic sea-level reconstructions for the penultimate deglaciation (blue line with 1σ uncertainty) and the last deglaciation (black line with 1σ uncertainty)[1]. Lower panel shows June 21 insolation for 65°N for the penultimate deglaciation (blue line) and the last deglaciation (black line)[7].

Extended Data Fig. 3. Comparison of our freshwater forcing during T-II with other estimates. (**a**) Our simulated changes in AMOC. (b) Our FW forcing. (**c**) Reconstruction of freshwater (FW) flux from sea-level reconstructions from Waelbroeck et al.[1]. (**d**) Reconstruction of FW flux from sea-level reconstructions from Marino et al.[3] (**e**) Our stack of ice-rafted for Heinrich event 11 (H11) (Extended Data Fig. 1), which shows that the H11 interval of iceberg

934 discharge is in good agreement with the timing of our FW forcing. (**f**) The sea-level change
935 associated with our FW flux into the North Atlantic (grey line), the sea-level change associated
936 with the ICE-5G ice sheets[33] used as a boundary condition in our climate model (green line), and
937 a reconstruction of global sea-level change[1] (blue line with 1 sigma uncertainty). The timing of
938 sea-level change in the ICE-5G time series shown here was adjusted from its chronology for T-I
939 by adjusting the corresponding sea-level rise to closely follow the Waelbroeck et al.[1] and Grant et
940 al.[34] sea-level reconstructions for the penultimate deglaciation.
941
942 **Extended Data Fig. 4. Maps of the evolution of temperature at 400-m water depth in the**
943 **North Atlantic, Arctic, and Southern Oceans between 138 ka and 124 ka relative to**
944 **temperature at 140 ka. a-h,** Maps of the evolution of temperature at 400-m water depth in the
945 North Atlantic and Arctic Oceans for (**a**) 138-140 ka, (**b**) 136-140 ka, (**c**) 134-140 ka, (**d**) 132-
946 140 ka, (**e**) 130-140 ka, (**f**) 128-140 ka, (**g**) 126-140 ka, and (**h**) 124-140 ka. **i-p,** Maps of the
947 evolution of temperature at 400-m water depth in the Southern Ocean for (**i**) 138-140 ka, (**j**) 136-
948 140 ka, (**k**) 134-140 ka, (**l**) 132-140 ka, (**m**) 130-140 ka, (**n**) 128-140 ka, (**o**) 126-140 ka, and (**p**)
949 124-140 ka.
950
951 **Extended Data Fig. 5. Predicted topography for the area covered by the Scandinavian Ice**
952 **Sheet at 131 ka.** The calculation is based on the LAM ice history (see text) and an Earth model
953 characterized by a lithosphere of thickness 100 km, upper mantle viscosity of 3 X 10^{20} Pa s, and
954 lower mantle viscosity of 5 X 10^{22} Pa s. The white zone in **(a)** represents coverage of grounded
955 ice extent at this time and the dashed white line on this frame is the shoreline location. Frame **(b)**
956 is identical to **(a)**, except the area of ice coverage is removed**.** It is clear from frame **(a)** that all

957 but the southeast section of the perimeter of the Scandinavian ice sheet is predicted to be marine
958 based at this time, and from frame (**b**) that much of the interior of the ice sheet was also marine
959 based.
960
961 **Extended Data Fig. 6. Results of sensitivity tests to oceanic forcing of the Greenland and**
962 **Antarctic ice sheets. (a)** Response of Greenland Ice Sheet to atmospheric forcing from CCSM3
963 with fixed ocean temperatures for the Penultimate Glacial Maximum (PGM) (blue line) and for
964 the Last Interglaciation (LIG) (orange line) compared to ice-sheet response to atmospheric and
965 oceanic forcing (black line). Present interglacial ice volume shown by horizontal dashed line. **(b)**
966 Response of Antarctic Ice Sheet to atmospheric forcing from CCSM3 with fixed ocean
967 temperatures for the PGM (blue line) and for the LIG (orange line) compared to ice-sheet response
968 to atmospheric and oceanic forcing (black line). Present interglacial ice volume shown by
969 horizontal dashed line. **(c)** As in **a**, response of Greenland Ice Sheet to atmospheric forcing from
970 CCSM3 with fixed ocean temperatures for the LIG (orange line), but the vertical scale (grounded
971 ice volume) has been increased to better illustrate the response. The initial ice-sheet size used in
972 this experiment (and the comparable one for Antarctica) was the LIG ice sheet, whereas the climate
973 forcing used was for the penultimate deglaciation and the LIG, i.e., from colder-than-present to
974 LIG climate, resulting in a small response to the atmospheric forcing, since the LIG ice-sheet size
975 had already adjusted to the combined atmospheric and oceanic forcing, as shown by the black line
976 in **a**.
977
978 **Extended Data Fig. 7. Predictions of relative sea level (RSL) at three far-field sites (the**
979 **Seychelles, Western Australia, and Mallorca) and one intermediate-field site (Bahamas). a-**

d, RSL predictions for the Bahamas from the full suite of simulations that bound from above all coral data with the exception of the earliest datum (at ~131 ka) for (**a**) the COL ice history, (**b**) the LAM ice history, (**c**) the HYB ice history, and (**d**) the WAE ice history. Age uncertainty is 2σ, and depth uncertainty reflects uncertainty in habitat depth. **e-h**, RSL predictions for the Seychelles from the full suite of simulations that lie above the three coral records with an elevation of ~4 m for (**e**) the COL ice history, (**f**) the LAM ice history, (**g**) the HYB ice history, and (**h**) the WAE ice history. Age uncertainty is 2σ, and depth uncertainty reflects uncertainty in habitat depth. **i-l**, RSL predictions for western Australia from the full suite of simulations that bound from above all coral data for (**i**) the COL ice history, (**j**) the LAM ice history, (**k**) the HYB ice history, and (**l**) the WAE ice history. Age uncertainty is 2σ, and depth uncertainty reflects uncertainty in habitat depth. **m-p**, RSL predictions for Mallorca from the full suite of simulations that fit the data within 50% of the minimum misfit achieved for all simulations for (**m**) the COL ice history, (**n**) the LAM ice history, (**o**) the HYB ice history, and (**p**) the WAE ice history. Age uncertainty is 2σ, and depth uncertainty reflects uncertainty in speleothem water depth.

Extended Data Fig. 8. Sensitivity of Greenland ice sheet model to melt parameterisation. (**a**) Time series of tuning experiments for the Greenland Ice Sheet with the preferred run in blue and three runs used for **b-d** shown in green, orange, and red. **b-d**. Surface elevation differences under a present-day climatology at the end of the 40,000-year T-I parameter tuning experiments, using degree-day factors drawn from our ensemble that (**b**), give a low amount of surface melting, (**c**), medium amount of surface melting, and (**d**), high amount of surface melting. Values shown are differences from the reference experiment. These experiments are identical to the T-I reference experiment used to parameterise the T-II simulations (Fig. 3) except for the degree-day factors

1003 used. The results show that our ice-sheet model is sensitive to the way in which surface mass
1004 balance is parameterised by controlling the amount of surface melting.
1005
1006 **Extended Data Fig. 9. Simulated ice-volume changes and components of the mass balance**
1007 **for the Greenland Ice Sheet.** (**a**) Simulated changes in ice volume for T-I. (**b**) Simulated changes
1008 in mass-balance components for T-I. (**c**) Simulated changes in ice volume for T-II. (**d**) Simulated
1009 changes in mass-balance components for T-II. (**e**) Modelled surface mass balance anomaly during
1010 the Last Interglaciation (129-120 ka) with respect to modelled present day.
1011
1012 **Extended Data Fig. 10. Comparison of our simulated summer temperature for Greenland**
1013 **ice-core sites with the temperature reconstructions for these sites based on $\delta^{18}O_{ice}$. (a)** The
1014 simulated summer temperature (JJA) (grey line) and lapse-rate corrected JJA temperature (green
1015 line) compared to reconstructed temperatures for the GISP2 ice-core site (blue symbols, 1 sigma
1016 uncertainty)[66,73] based on the relation $d\delta^{18}O_{ice}/dT$ = ~0.5‰ C^{-1} which is derived from Greenland
1017 ice-core sites elsewhere[74]. Also shown are the reconstructed temperatures using the $d\delta^{18}O_{ice}/dT$
1018 relation established for the NEEM site (~1.1‰ C^{-1})[75] (red symbols, 1 sigma uncertainty),
1019 suggesting that the GISP2 LIG summer temperatures are about half of the originally published
1020 values based on the Vinther et al.[74] $d\delta^{18}O_{ice}/dT$ relation and in good agreement with our model
1021 results. **(b)** The simulated JJA temperature (grey line) and lapse-rate corrected JJA temperature
1022 (green line) compared to reconstructed temperatures for the NEEM ice-core site (dark blue line,
1023 gray shading is uncertainty)[65] based on the relation $d\delta^{18}O_{ice}/dT$ = ~0.5‰ C^{-1} which is derived from
1024 Greenland ice-core sites elsewhere[74]. Also shown are the reconstructed temperatures using the
1025 $d\delta^{18}O_{ice}/dT$ relation established for the NEEM site (~1.1‰ C^{-1})[75] (red line, pink shading is

1026 uncertainty), suggesting that the NEEM LIG summer temperatures are about half of the originally
1027 published values based on the Vinther et al.[74] $d\delta^{18}O_{ice}/dT$ relation and in good agreement with our
1028 model results. These reconstructions span the interval 127-120 ka, which is the warmest interval
1029 in the ice-core records for the LIG suggested by this proxy.

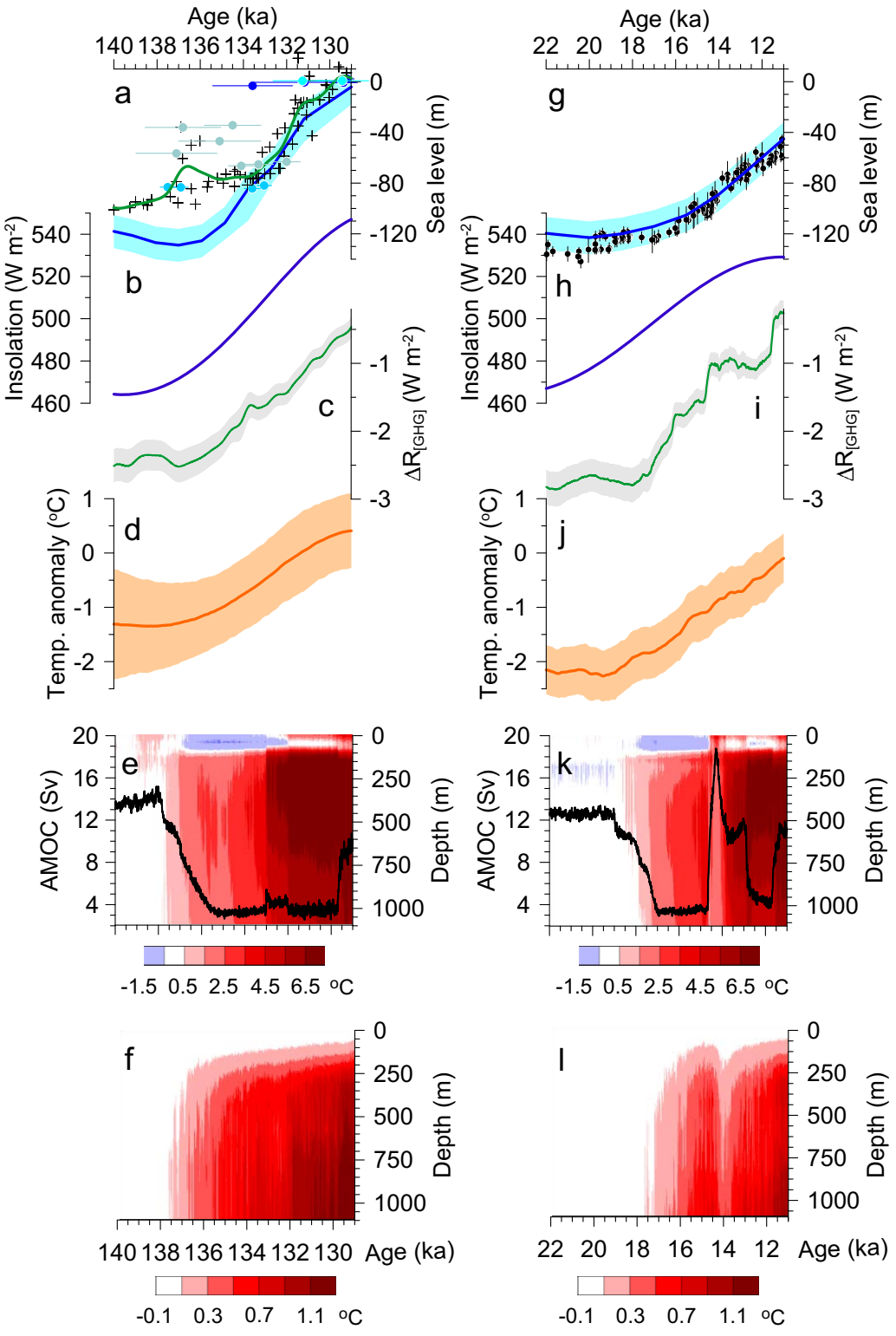
Age (ka)
140 138 136 134 132 130
22 20 18 16 14 12
a
g
Sea level (m)
0
-40
-80
-120
b
h
Insolation (W m-2)
540
520
500
480
460
c
i
ΔR[GHG] (W m-2)
-1
-2
-3
d
j
Temp. anomaly (°C)
1
0
-1
-2
e
k
AMOC (Sv)
20
16
12
8
4
Depth (m)
250
500
750
1000
-1.5 0.5 2.5 4.5 6.5 °C
f
l
-0.1 0.3 0.7 1.1 °C

Figure 1

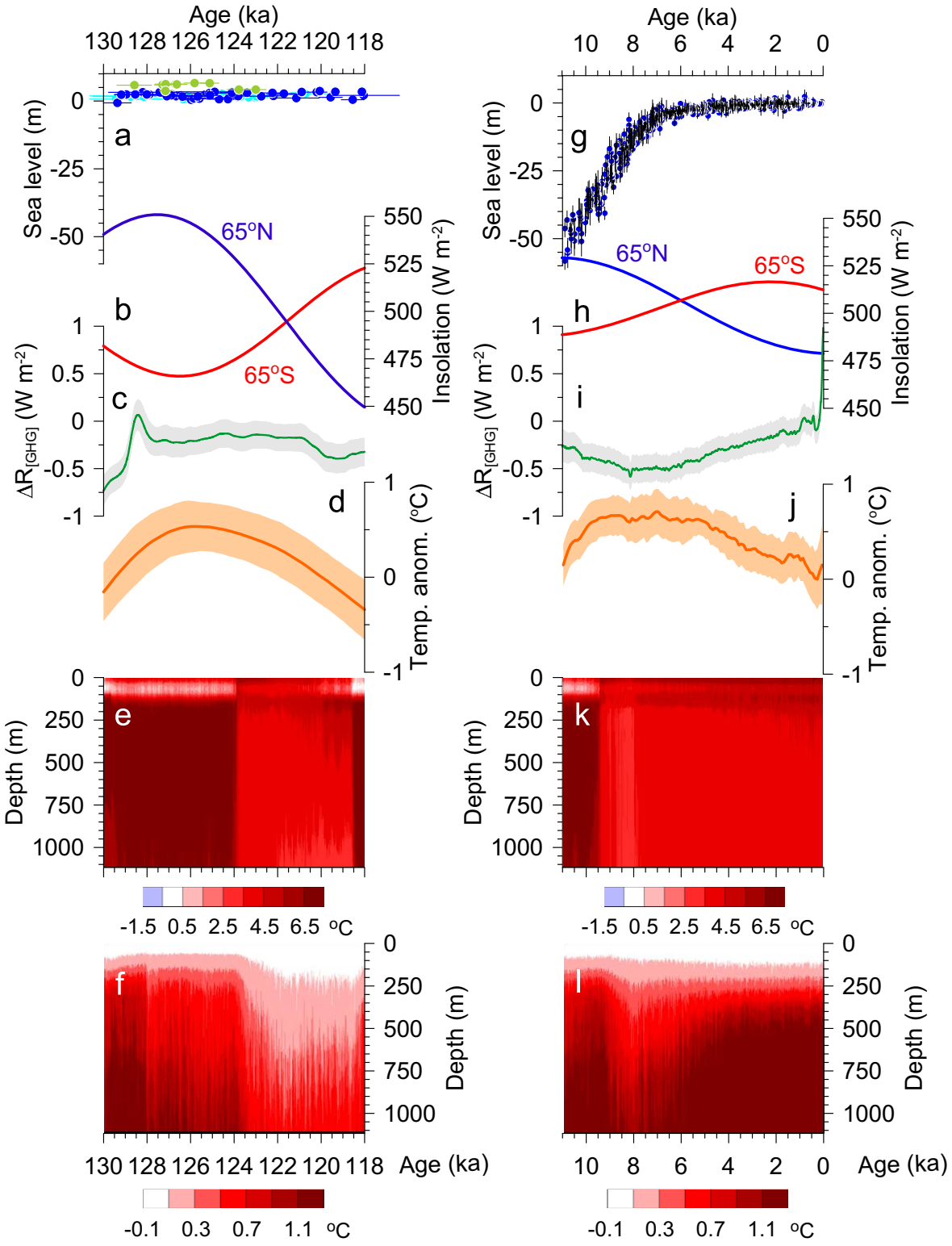
Age (ka)
130 128 126 124 122 120 118
Sea level (m)
0
-25
-50
a
65°N
65°S
b
1
0.5
0
-0.5
-1
ΔR[GHG] (W m-2)
c
550
525
500
475
450
Insolation (W m-2)
d
1
0
-1
Temp. anom. (°C)
e
Depth (m)
0
250
500
750
1000
-1.5 0.5 2.5 4.5 6.5 °C
f
130 128 126 124 122 120 118 Age (ka)
-0.1 0.3 0.7 1.1 °C
Age (ka)
10 8 6 4 2 0
g
h
i
j
k
l

Figure 2

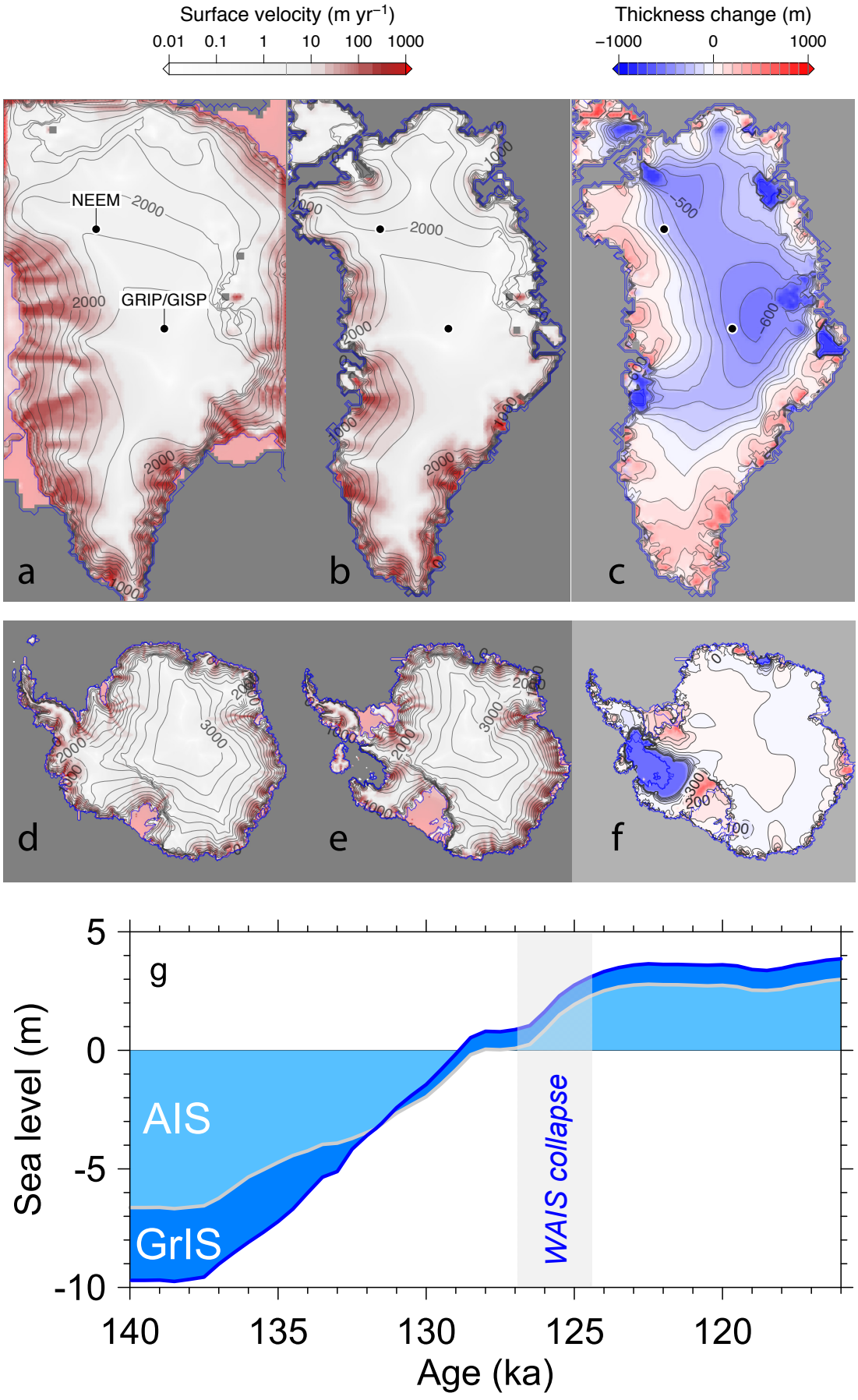
Surface velocity (m yr^{-1})
0.01 0.1 1 10 100 1000
Thickness change (m)
−1000 0 1000
NEEM
GRIP/GISP
a
b
c
d
e
f
g
Sea level (m)
5
0
-5
-10
AIS
GrIS
WAIS collapse
140 135 130 125 120
Age (ka)

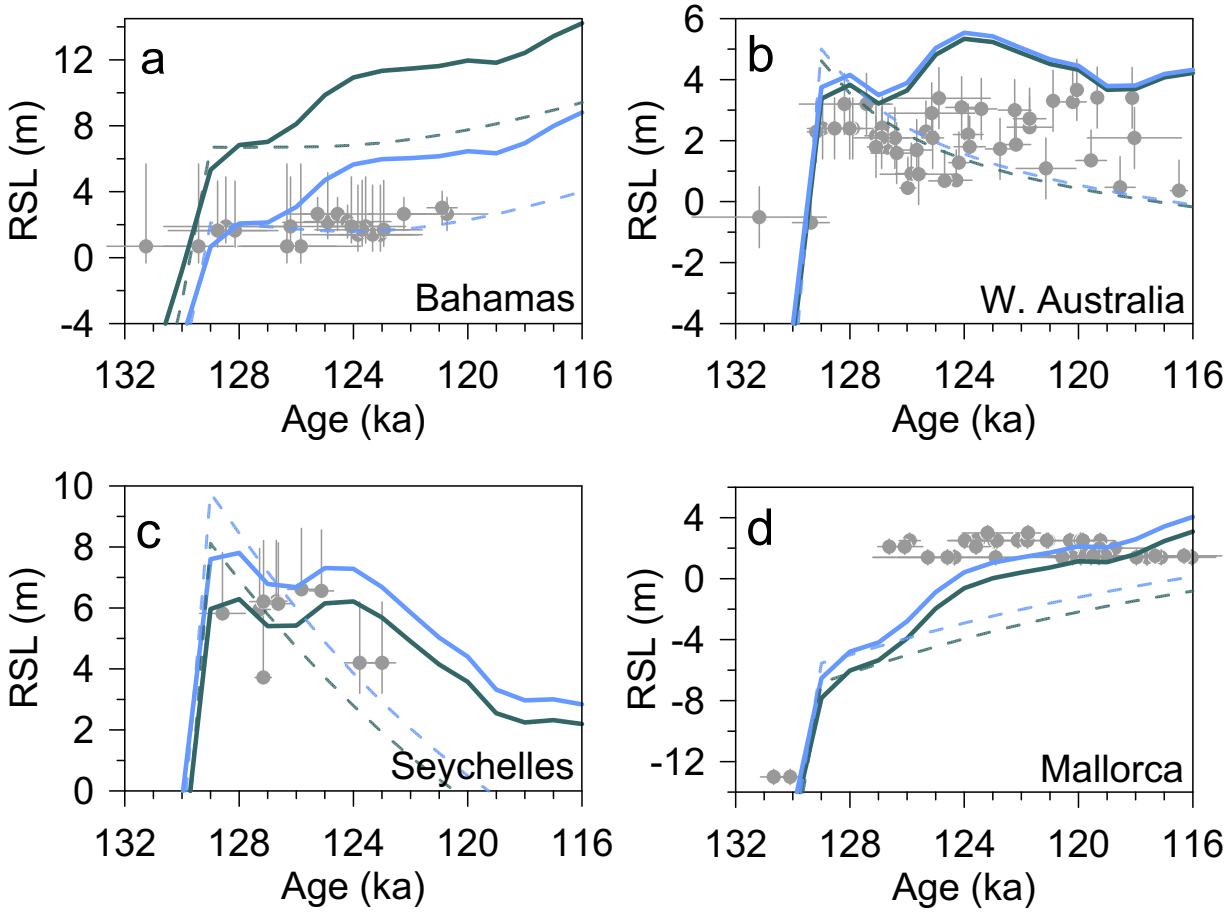
a
Bahamas
b
W. Australia
c
Seychelles
d
Mallorca
RSL (m)
Age (ka)
132
128
124
120
116

Figure 4

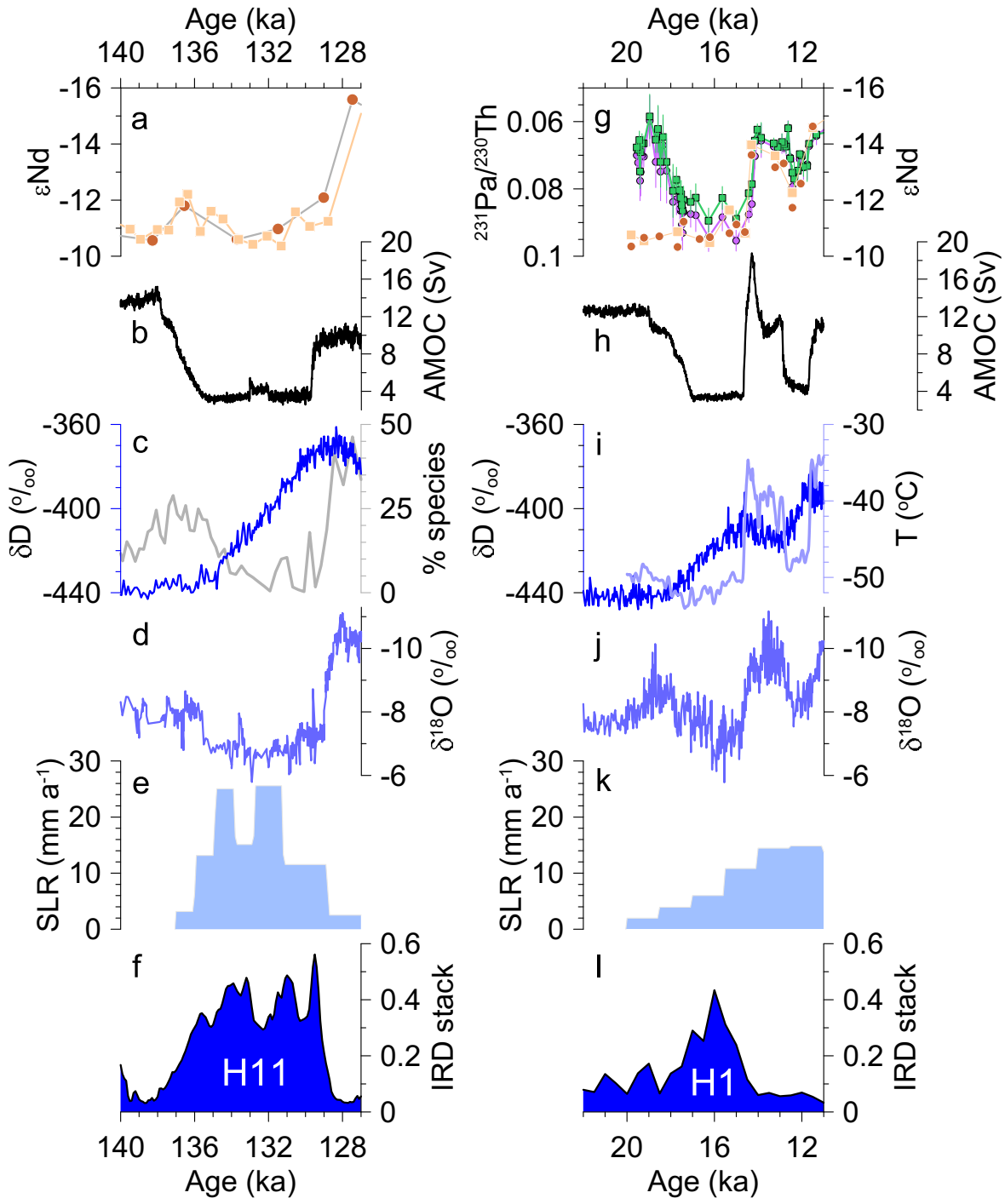
Age (ka)
140
136
132
128
-16
-14
-12
-10
εNd
a
b
20
16
12
8
4
AMOC (Sv)
-360
-400
-440
δD (‰)
c
50
25
0
% species
d
-10
-8
-6
δ18O (‰)
30
20
10
0
SLR (mm a-1)
e
f
0.6
0.4
0.2
0
IRD stack
H11
Age (ka)
20
16
12
231Pa/230Th
0.06
0.08
0.1
g
h
i
-30
-40
-50
T (°C)
j
k
l
H1

ED Fig. 1

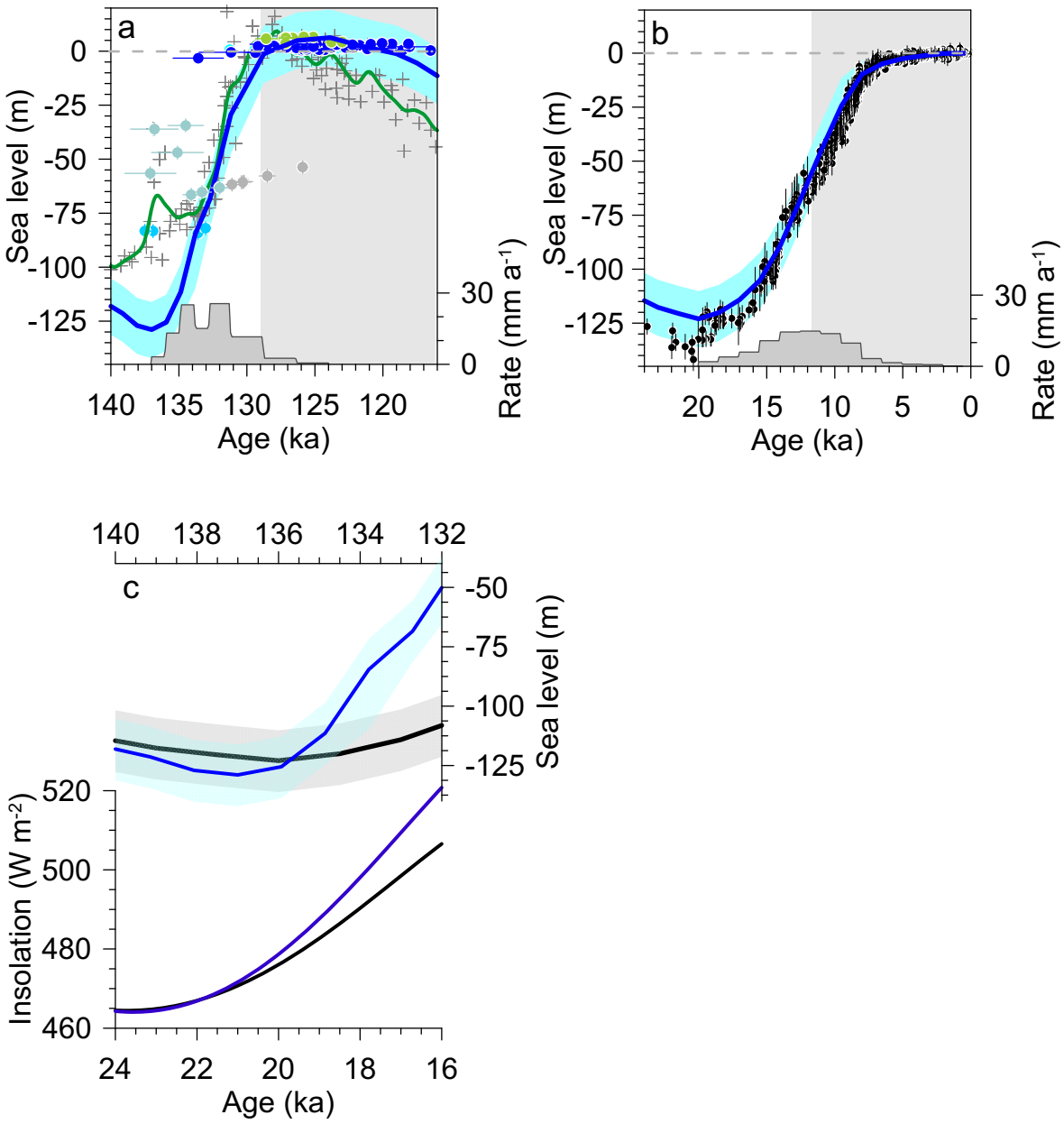
a
b
c
Sea level (m)
Rate (mm a-1)
Age (ka)
Insolation (W m-2)
0
-25
-50
-75
-100
-125
30
140
135
130
125
120
20
15
10
5
138
136
134
132
520
500
480
460
24
22
18
16

ED Fig. 2

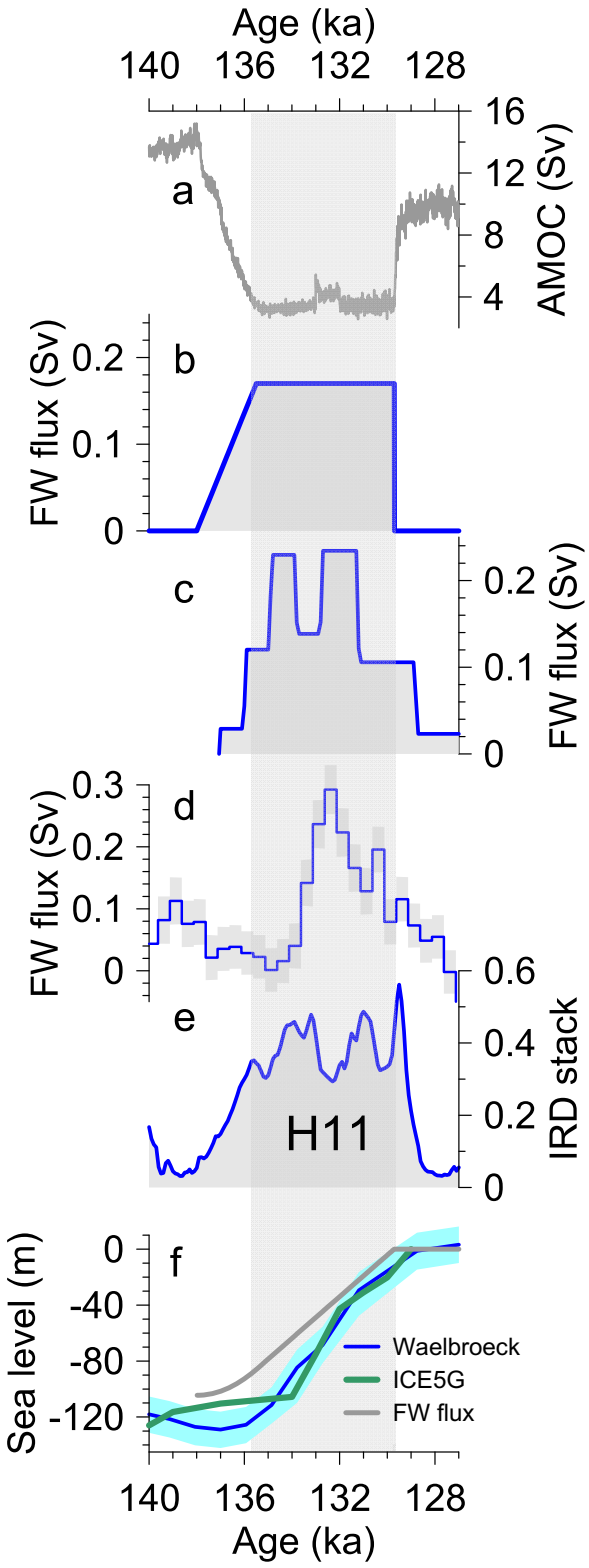
Age (ka)
140
136
132
128
16
12
8
4
AMOC (Sv)
a
b
FW flux (Sv)
0.2
0.1
0
c
FW flux (Sv)
d
0.3
e
H11
0.6
0.4
IRD stack
f
Sea level (m)
-40
-80
-120
Waelbroeck
ICE5G
FW flux

ED Fig. 3

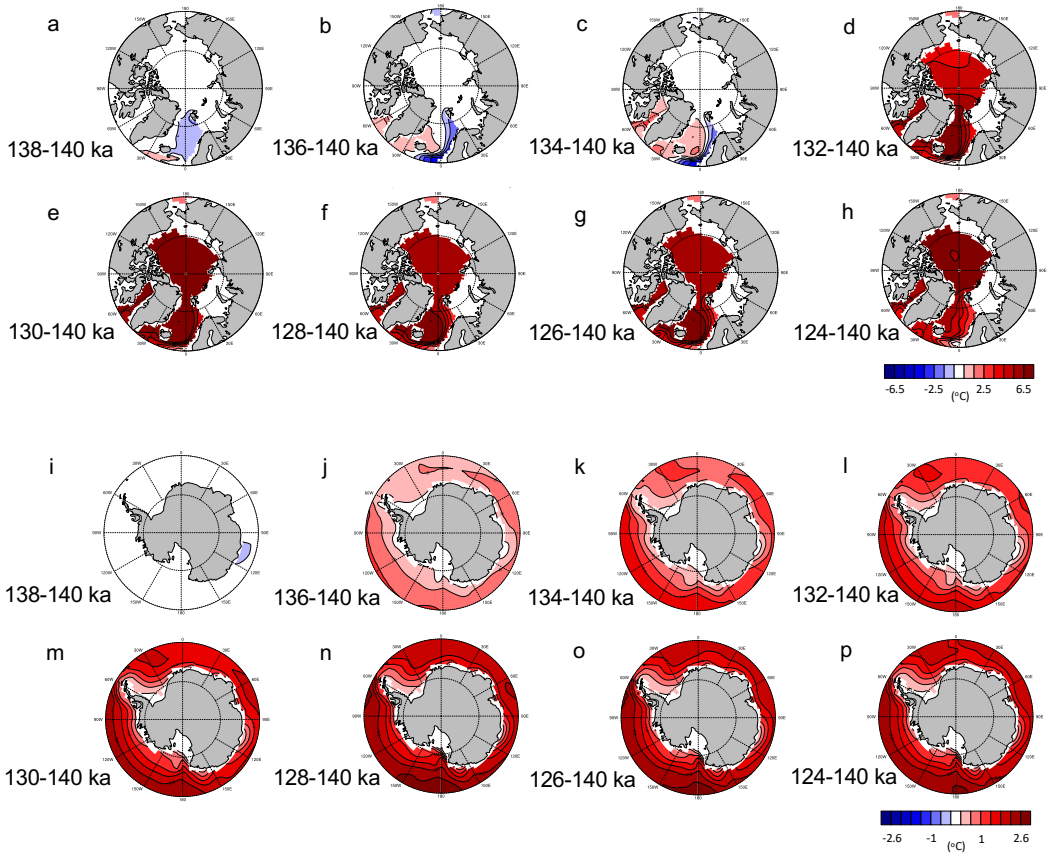
a
138-140 ka
b
136-140 ka
c
134-140 ka
d
132-140 ka
e
130-140 ka
f
128-140 ka
g
126-140 ka
h
124-140 ka
-6.5
-2.5
(°C)
2.5
6.5
i
138-140 ka
j
136-140 ka
k
134-140 ka
l
132-140 ka
m
130-140 ka
n
128-140 ka
o
126-140 ka
p
124-140 ka
-2.6
-1
(°C)
1
2.6

ED Fig. 4

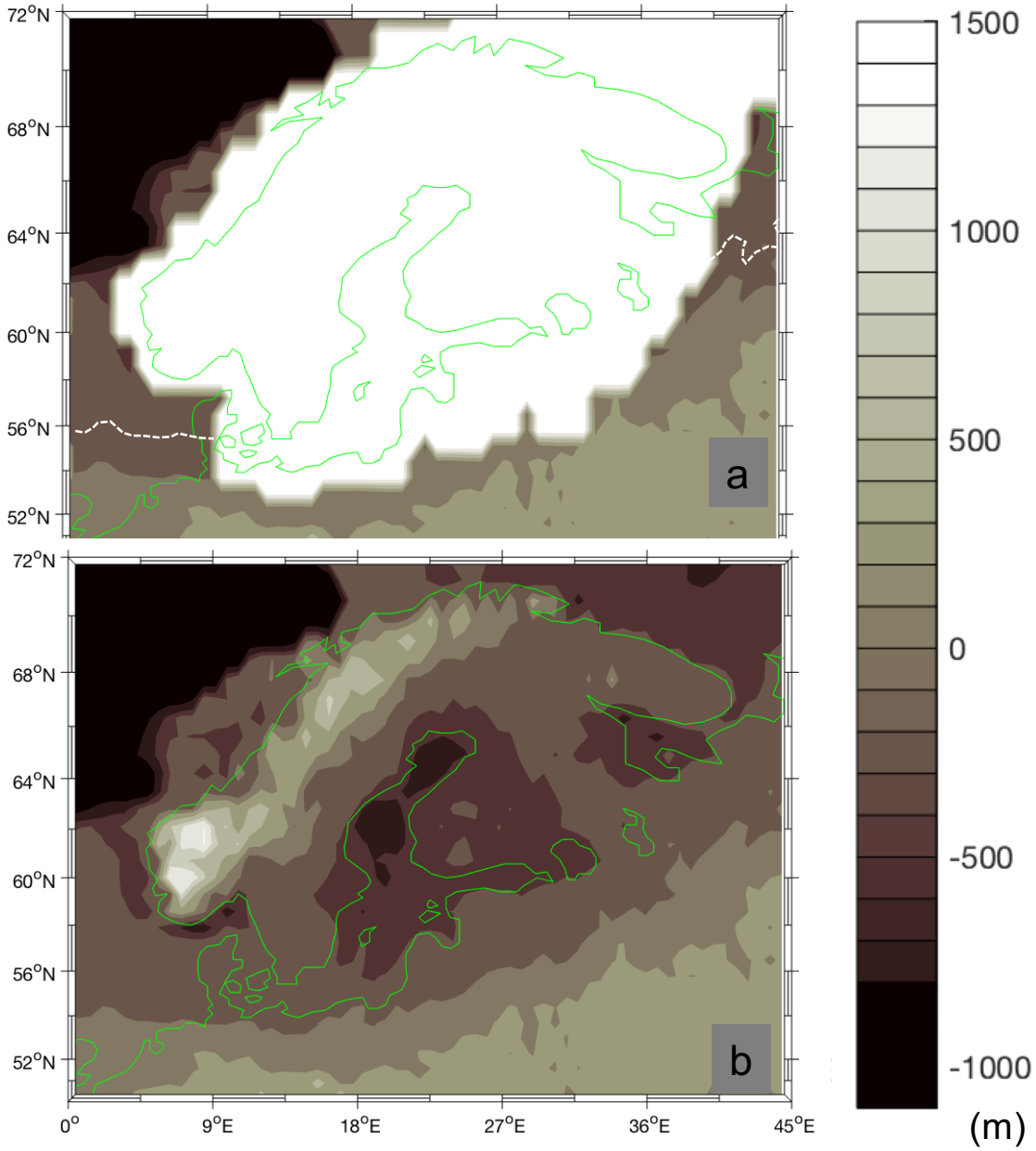
72°N
68°N
64°N
60°N
56°N
52°N
a
b
0°
9°E
18°E
27°E
36°E
45°E
1500
1000
500
0
-500
-1000
(m)

ED Fig. 5

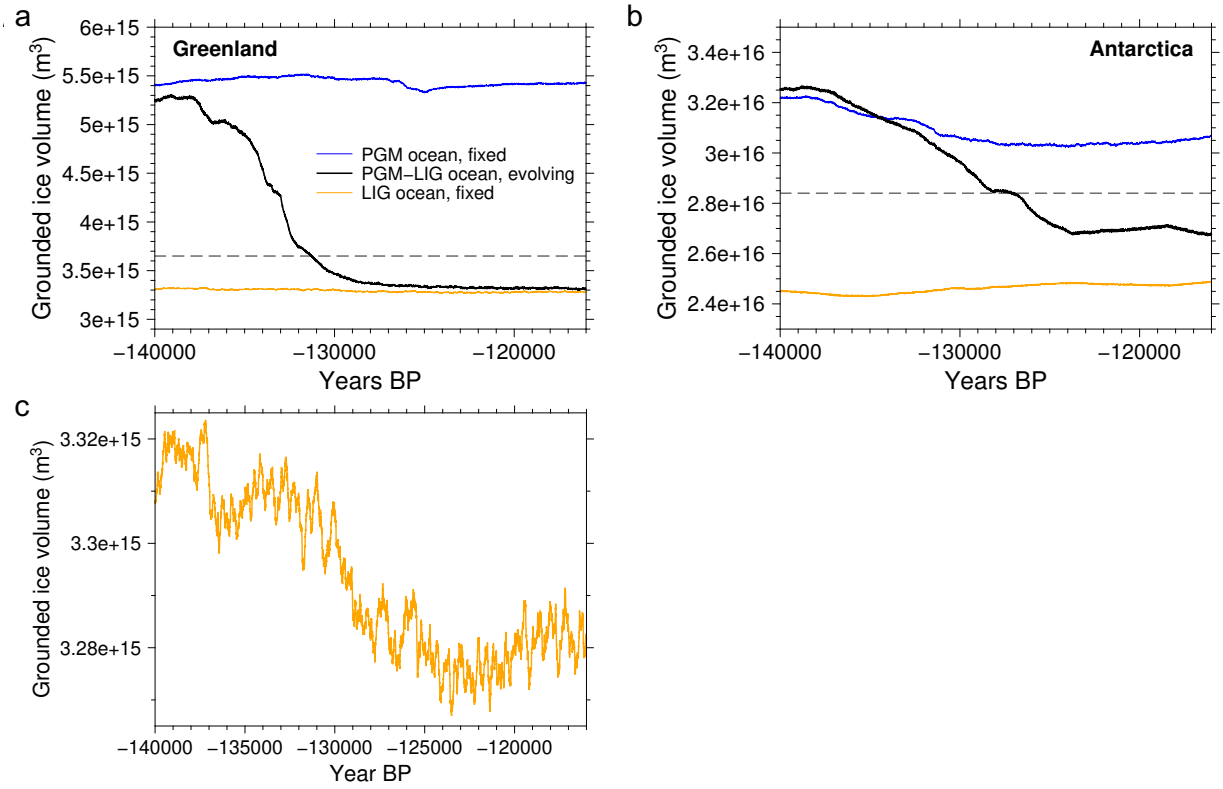
a
Greenland
Grounded ice volume (m3)
6e+15
5.5e+15
5e+15
4.5e+15
4e+15
3.5e+15
3e+15
PGM ocean, fixed
PGM–LIG ocean, evolving
LIG ocean, fixed
−140000
−130000
−120000
Years BP
b
Antarctica
Grounded ice volume (m3)
3.4e+16
3.2e+16
3e+16
2.8e+16
2.6e+16
2.4e+16
−140000
−130000
−120000
Years BP
c
Grounded ice volume (m3)
3.32e+15
3.3e+15
3.28e+15
−140000
−135000
−130000
−125000
−120000
Year BP

ED Fig. 6

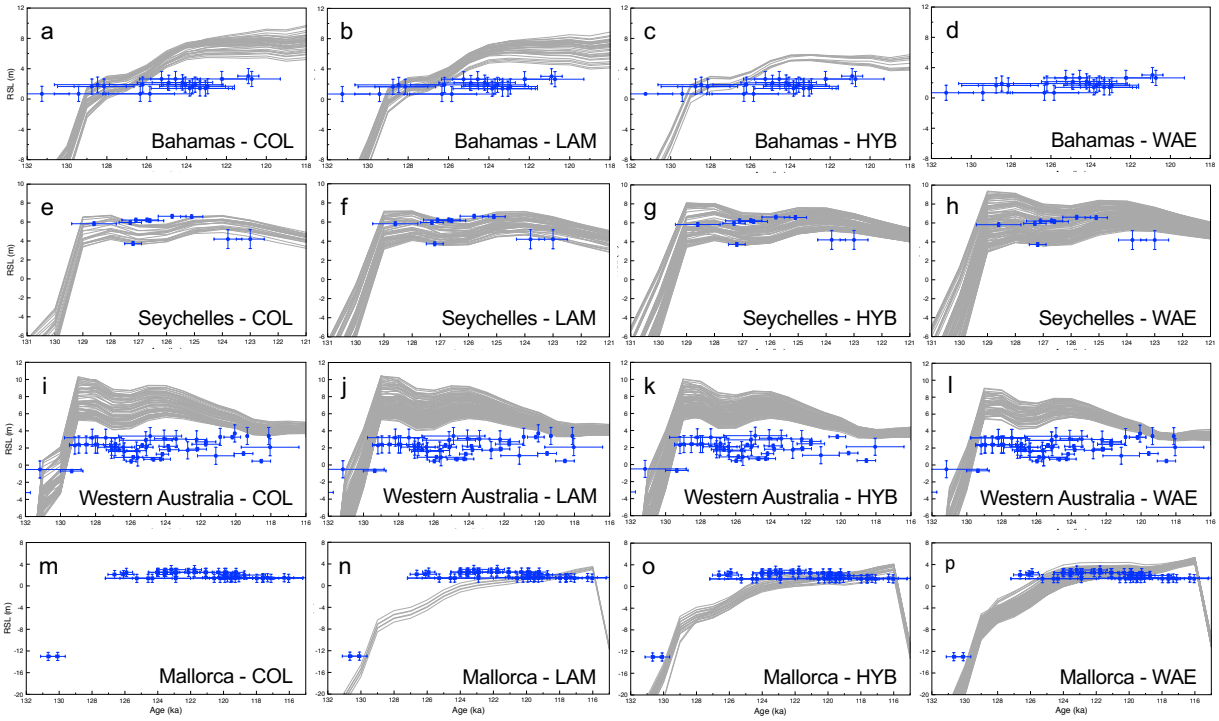
a
Bahamas - COL
b
Bahamas - LAM
c
Bahamas - HYB
d
Bahamas - WAE
e
Seychelles - COL
f
Seychelles - LAM
g
Seychelles - HYB
h
Seychelles - WAE
i
Western Australia - COL
j
Western Australia - LAM
k
Western Australia - HYB
l
Western Australia - WAE
m
Mallorca - COL
n
Mallorca - LAM
o
Mallorca - HYB
p
Mallorca - WAE
RSL (m)
Age (ka)

ED Fig. 7

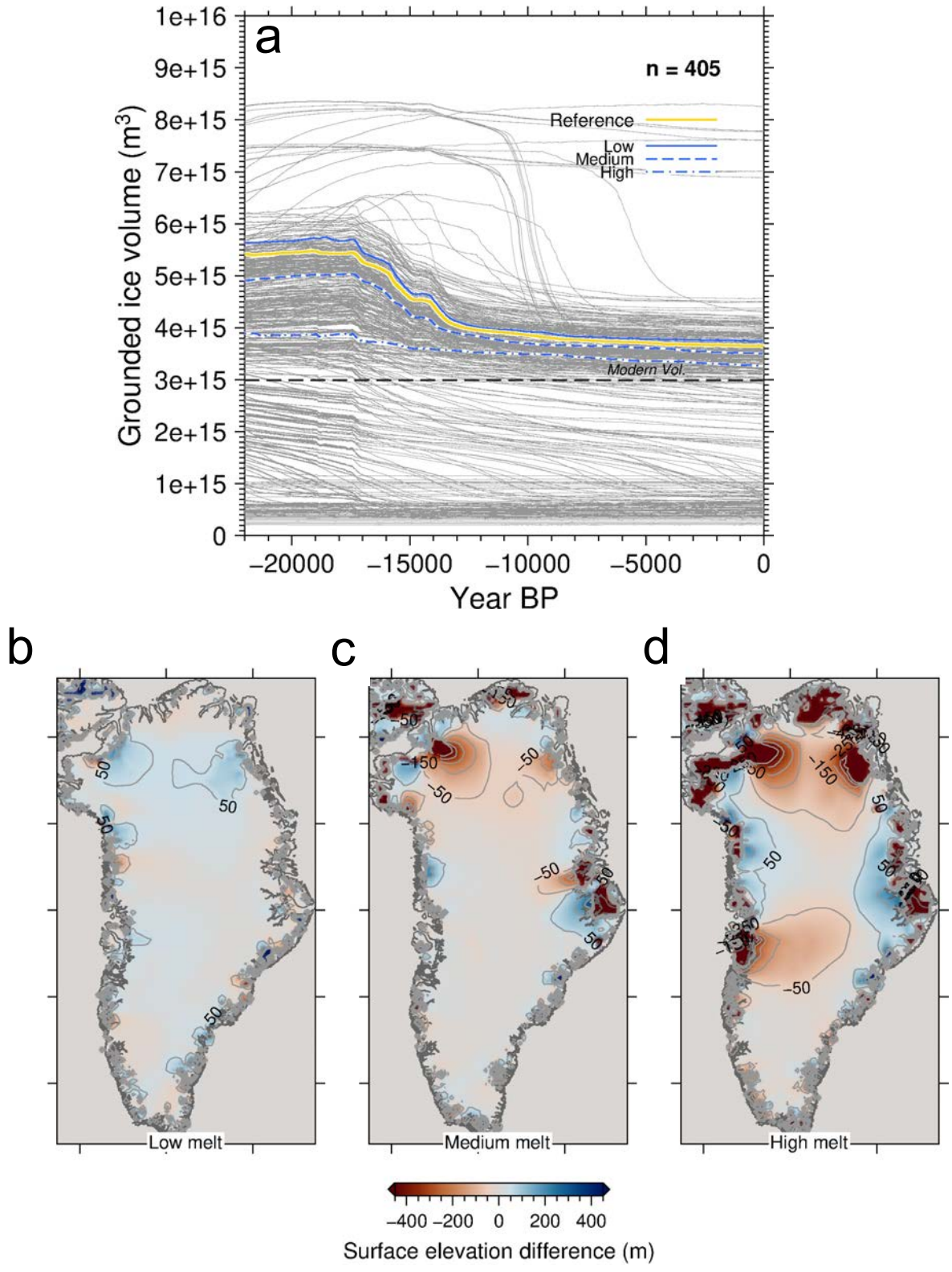
a
n = 405
Reference
Low
Medium
High
Modern Vol.
Grounded ice volume (m3)
1e+16
9e+15
8e+15
7e+15
6e+15
5e+15
4e+15
3e+15
2e+15
1e+15
0
−20000
−15000
−10000
−5000
0
Year BP
b
c
d
Low melt
Medium melt
High melt
−400 −200 0 200 400
Surface elevation difference (m)

ED Fig. 8

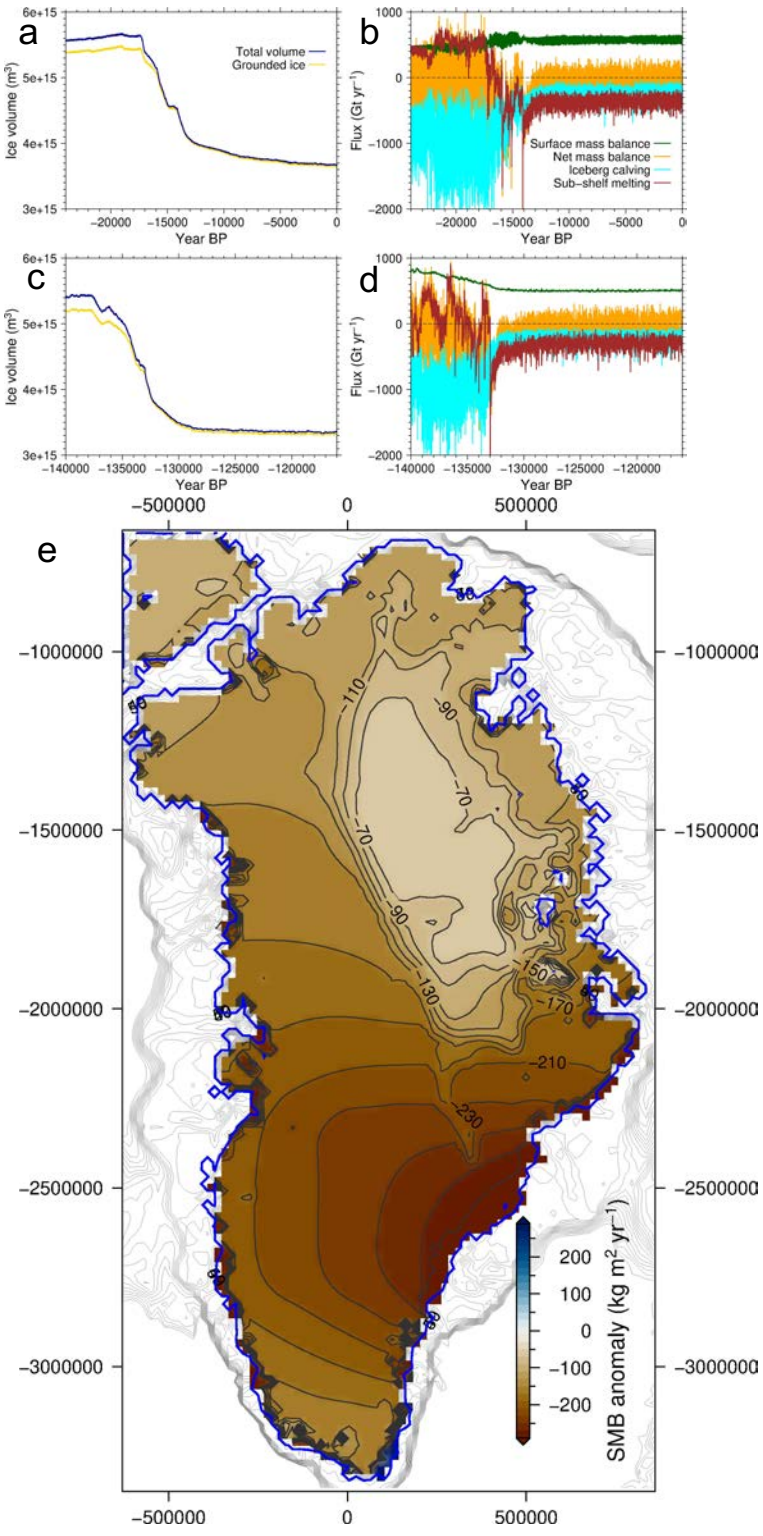
a
b
c
d
e
Ice volume (m³)
Flux (Gt yr⁻¹)
Year BP
Total volume
Grounded ice
Surface mass balance
Net mass balance
Iceberg calving
Sub−shelf melting
SMB anomaly (kg m² yr⁻¹)

ED Fig. 9

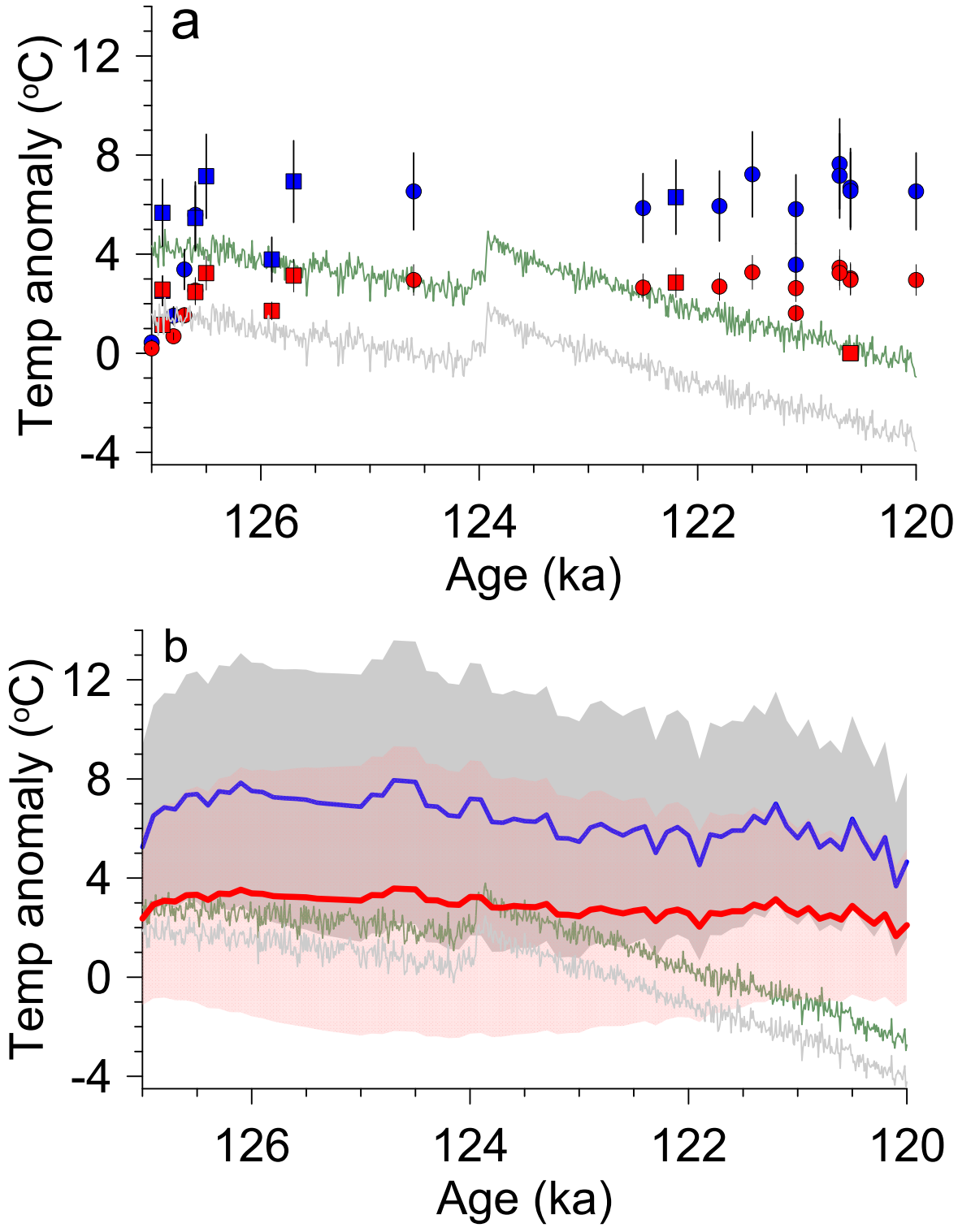
a
Temp anomaly (°C)
12
8
4
0
-4
126
124
122
120
Age (ka)
b
Temp anomaly (°C)
12
8
4
0
-4
126
124
122
120
Age (ka)

ED Fig. 10